Available online at www.sciencedirect.com

SCIENCE @ DIRECT®

Journal of Computational Physics 194 (2004) 451–480

JOURNAL OF
COMPUTATIONAL
PHYSICS

www.elsevier.com/locate/jcp

An indirect boundary element method for three-dimensional explosion bubbles

C. Wang [a], B.C. Khoo [b,c,*]

[a] Institute of High Performance Computing, 1 Science Park Road, #01-01 The Capricorn, Singapore Science Park II, Singapore 117528, Singapore
[b] Department of Mechanical Engineering, National University of Singapore, 10 Kent Ridge Crescent, Singapore 119260, Singapore
[c] Singapore MIT Alliance, 4 Engineering Drive 3, Singapore 117576, Singapore

Received 17 March 2003; received in revised form 5 August 2003; accepted 9 September 2003

Abstract

This paper suggests the implementation of indirect boundary element method (IBEM) to simulate three-dimensional underwater explosion bubbles. The source is assumed distributed continuously on the boundary surface. An expression for the self-induced velocity of a point on the boundary surface is obtained via mathematical analysis, and with it a new definition of the normal vector valid even for a non-smooth surface is given. Elastic mesh technique (EMT), which is a new mesh regulation technique, is further applied to maintain the regularity of the triangular-element mesh used to discretize the dynamic boundary surfaces during the evolution of explosion bubble(s). The Bi-CG iterative solver is employed to solve the resulting linear system. All these efforts make the present approach viable and robust, and which is validated by computations of several bubble dynamics problems.

PACS: 65N38; 76Bxx

Keywords: Indirect boundary element method; Elastic mesh technique; Bi-CG iterative solver; Underwater explosion bubble

---

1. Introduction

Boundary element method (BEM) is commonly applied in the simulation of bubble(s) dynamics and can be partly attributed to the inherent property of reducing the dimension of the problem by one, which greatly conserves computational effort. This can become a critical issue in the simulation of three-dimensional multiple bubbles in the presence of more complex geometrical solid boundaries and/or free surface. The employment of BEM to bubble dynamics can be seen in the early work of Blake and Gibson [3] who studied

---

* Corresponding author. Tel.: +65-874-2889; fax: +65-779-1459.
E-mail address: mpekbc@nus.edu.sg (B.C. Khoo).

doi:10.1016/j.jcp.2003.09.011

the growth and collapse of a vapor cavitation near a free surface. Their numerical results of the bubble shape as it evolved matched well with the experiment, which suggests that BEM can be a good approach to capture the complex features of bubble dynamics including the formation of water jet. In their later work of Blake and Gibson [4], the same methodology is used to investigate the evolution of a cavity bubble near a solid wall. They also introduced a new criterion to decide the proper time step size for evolution of the bubble dynamics, which is widely used now. Other works employing BEM to study bubble dynamics include Oguz and Prosperetti [11] investigation of the entrained bubbles produced by the impact of drops on surface of the same liquid, and Lundgren and Mansour [10] study of an initially spherical bubble rising in a gravity field. The simulation started from a spherical bubble till its jet is closed to making an impact on the upper surface. Then a toroidal bubble, whose size and rotation is estimated based on the earlier computed results, was simulated and followed on. In still other works, Harris [9] simulated the three-dimensional motion of a bubble close to a fixed rigid spherical ball and cylinder. Harris used 4-node elements with linear base function to construct the bubble and structure surface. In further development of a more accurate calculation pertaining to the formation of the toroidal cavity bubble near a rigid boundary, Best [1] introduced a branch cut and formulated a boundary integral equation valid for both on the bubble surface and the branch cut. This approach was adopted and led to Zhang et al. [17] simulation of an initially spherical cavity bubble which is located near a rigid wall till its full toroidal phase. In these said works, a contact interface was defined to separate the water jet and the surrounding domain during the toroidal bubble phase. Following, Zhang and Duncan [16] extended the study to adiabatic gas bubble and which overcome the issue related to the presence of extremely high pressure during bubble collapse as encountered for their previous cavity bubble model. In more recent years, Wang et al. [14] continued to employ BEM to study the non-linear interaction between a gas bubble and free surface. They first employed a surgical-cut to convert the bubble to a toroidal shape and then used a vortex ring inside bubble to model the rotational part of the flow. Tong [12] also numerically investigated the three-dimensional interaction of transient cavities in fluid flows with rigid boundaries, which include spherical and oval balls. Zhang et al. [18] carried out computations involving several different configurations of two three-dimensional bubbles in the presence of a nearby free surface. A follow-on work by Zhang et al. [20] then extended the surgical-cut to three-dimensional toroidal bubble problems. In essence, BEM has been extensively used for the study of the bubble dynamics problems.

Thus far, it is fair to say that most simulations of three-dimensional bubble dynamics are primarily based on the so-called direct boundary element method (DBEM) in which the potential or its normal derivative is the primary unknown to be solved first. The material velocity of the bubble surface is then calculated by combining the normal velocity component which is obtained based on the definition of the normal direction on the described surface by some global or local surface interpolation schemes, and the tangential velocity components which are determined by evaluating the tangential derivatives of the potential along the bubble surface. Harris [9] suggested an averaging of linear approximations on the surface element. However as noted by Blake et al. [2], this algorithm suffers from non-convergence under mesh refinement. Chahine et al. [8], on the other hand, used quadratic polynomials to fit the surface locally. However, as also noted by Blake et al. [2], the method fails for certain arrangements of the nodes and is thus not considered very robust. Blake et al. [2] proposed the use of radial basis functions since it was purported to be universally applicable. However, since the interpolation scheme via radial basis functions is based on a bivariated representation $z = f(x, y)$ of the surface, a new orientation of Cartesian axes must be chosen once a part of the bubble surface becomes parallel (or almost parallel) to the z-axis. Finally, Zhang et al. [18] introduced a trivariated interpolation scheme based on the 9-node Lagrangian element, but in their recent followed-on work [19] they agreed that this approach might be cumbersome if mesh refinement is carried out as the bubble evolves or when the bubble undergoes topological changes from a singly connected region to a doubly connected region.

Indirect boundary element method (IBEM) takes the source or dipole distributions as the primary unknown and which are solved first. The potential and material velocity in the flow field can then be evaluated by integration over the singularity distributed region. Interpolation and calculation of the derivatives of potential along bubble surface are unnecessary in the indirect approach, which implies that the indirect methods can be potentially more accurate and suitable for numerical implementation. Most applications of the indirect methods, however, are for the axisymmetric and two-dimensional bubbles. Blake and Gibson [3] used a discrete ring source distribution to (approximately) represent the cavitation bubble and the adjacent free surface. Boulton-Stone [6] tried both source and dipole distribution methods. One major difficulty of IBEM lies in calculating the material velocity which can give rise to some hyper-singular integrals leading to uncertainty in interpretation in the sense of the Cauchy principal value. Boulton-Stone [6] overcame this problem by proposing the use of quadratic fitting of the bubble boundary. This, however, seemingly only removes the difficulty but results in a much smaller velocity once the singularity is smoothed out. In fact, it is reckoned that this was responsible for the abnormally early breakdown of the said method. Further more, the proposed solution by Boulton-Stone where surface fitting is required becomes less attractive compared to the direct formulation. Finally, Zhang et al. [19] proposed a desingularized indirect BEM method. In this case, the singularity was distributed not on the bubble surface, but a certain distance inside the bubble. However, this method has the limitation that towards the final phase of the jet impact on the opposite bubble surface, the computation becomes extremely slow. In addition, one can easily foresee problems relating to the placement of the distributed singularity when the bubble surfaces come increasingly close to each other and eventually meet and evolve into toroidal form.

The present paper proposes an IBEM in which the source is continuously distributed along the bubble surface. This approach can theoretically prevent the appearance of any singularity in potential and velocity evaluation, as long as all boundaries are smooth. The formulation for the self-induced velocity of a point on the bubble surface is derived. Based on that, the normal vector with respect to the bubble surface is defined and which is valid even for a non-smooth surface. In the implementation, triangular-element discrete surface is constructed to represent the dynamic bubble boundary, and a linearly distributed source is in turn defined for each triangular element on the bubble surface. All quadratures involved in the evaluation of influence matrix and the calculation of potential/velocity unknowns are carried out by accurate formulae. When this method is used initially to simulate a bubble with jet formation, most of the surface elements are found to gather at the location of jet tip and its vicinity leading to problem associated with overcrowding and presence of many small elements. This problem can be alleviated with the application of elastic mesh technique (EMT) introduced recently [13]. EMT is employed judiciously to better distribute the elements on the bubble surface(s) and yet is able to capture the ensuing jet formation; its application has obviated the need or delay the employment of mesh refinement/deletion. Finally, the Bi-CG solver which is more efficient than the traditional Gauss elimination matrix solver is adopted to solve the resulting linear system.

2. Mathematical formulae

2.1. Potential theory

Source (and sink) is commonly applied to solve potential flows of zero lift problems. The potential and velocity at point P induced by a point source located at point Q with unit strength can be formulated as follows:

$$\phi^* = -\frac{1}{r}, \tag{1a}$$

$$\vec{v}^{\,*} = \frac{\vec{r}}{r^3}, \tag{1b}$$

where $\vec{r}$ is the vector from point Q to P. Eqs. (1a) and (1b) are very simple, but it is not suitable to use point source directly in numerical calculation since singularity occurs when P approaches Q. One cannot, therefore, obtain the values of potential and velocity at the source point Q. A continuous distribution of the source on the boundary surface is a way to weaken the singularity significantly. As long as both the boundary surface and the source distribution are smooth, the induced potential and velocity will have limited values on boundary as well as in the domain.

The flow domain is denoted by Ω, which is bounded by surface S. On the surface the source density σ is continuously distributed. The vectors from the origin O to point P and Q are given by $\vec{r}_P$ and $\vec{r}_Q$, respectively. $\vec{r}$ is the vector from Q to P, i.e.

$$\vec{r} = \vec{r}_P - \vec{r}_Q. \tag{2}$$

If point P is located inside the domain Ω (not on the surface S), then the total potential and velocity at point P induced by all the sources distributed continuously on surface S can be evaluated by integration over S (see Fig. 1), i.e.

$$\phi(P) = -\iint\limits_S \frac{\sigma(Q)}{r(P,Q)} \mathrm{d}s(Q), \tag{3a}$$

$$\vec{v}(P) = \iint\limits_S \frac{\sigma(Q)\vec{r}(P,Q)}{r^3(P,Q)} \mathrm{d}s(Q). \tag{3b}$$

If point P is located on the surface S (see Fig. 2), Eqs. (3a), (3b) cannot be applied directly since the associated integral kernels are singular. Limiting analysis must be used for the evaluation. Consider a sphere of radius $\varepsilon > 0$, with its center coinciding with the point P on surface S. When ε is sufficiently small, the surface of the sphere is cut into two portions, with the portion lying outside of the flow domain Ω denoted by S_ε. The original surface S is also divided into two parts, of which the part lying inside the sphere is denoted by S_c. S_ε and S_c share the same boundary curve. On surface S (including S_c) the unit normal $\vec{n}$ is defined pointing to the outside of Ω. On S_ε the unit normal $\vec{n}$ is defined pointing to the outside of the sphere (see Fig. 2). With a new surface taken to be $S' = S - S_c + S_\varepsilon$ of which the point P is excluded, we evaluate the values of potential and velocity at point P using Eqs. (3a) and (3b):

$$\phi(P) = -\iint\limits_{S-S_c} \frac{\sigma(Q)}{r(P,Q)} \mathrm{d}s(Q) - \iint\limits_{S_\varepsilon} \frac{\sigma(Q)}{\varepsilon} \mathrm{d}s(Q), \tag{4a}$$

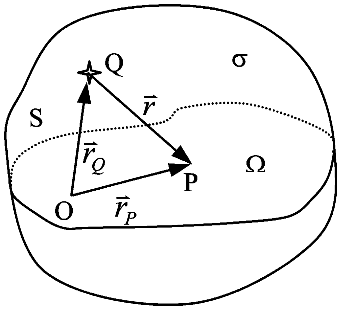

Fig. 1. Geometry configuration.

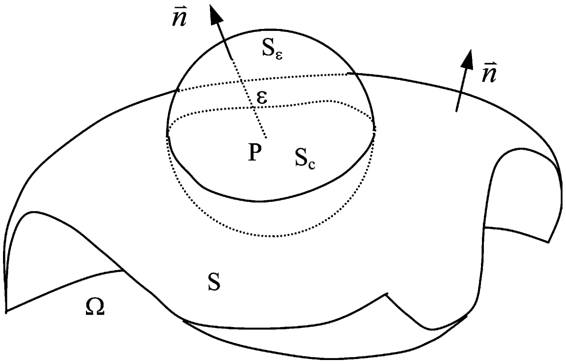

Fig. 2. Configuration of limiting analysis process.

$$\vec{v}(P) = \iint\limits_{S-S_c} \frac{\sigma(Q)\vec{r}(P,Q)}{r^3(P,Q)}\mathrm{d}s(Q) + \iint\limits_{S_\varepsilon} \frac{\sigma(Q)\vec{r}(P,Q)}{\varepsilon^3}\mathrm{d}s(Q), \tag{4b}$$

when $\varepsilon \to 0$, S_ε and $S_c \to 0$, $S' = S - S_c + S_\varepsilon \to S$. Therefore, the potential and velocity at point P which is located on surface S can be evaluated by limiting $\varepsilon \to 0$ in Eqs. (4a) and (4b). The solid angle subtended at point P by surface S is given as

$$\Theta = \lim_{\varepsilon\to 0} \frac{1}{\varepsilon^2} \iint\limits_{S_\epsilon} \mathrm{d}s. \tag{5a}$$

Here Θ is a real number varying between *0* and 4π. The gravity center of the surface S_ε can be evaluated as

$$\vec{r_c} = \frac{\iint\limits_{S_\varepsilon} \vec{r_Q}\,\mathrm{d}s(Q)}{\iint\limits_{S_\varepsilon} \mathrm{d}s(Q)}. \tag{5b}$$

As such, when $\varepsilon \to 0$, $\vec{r_c} \to \vec{r_P}$. Also noting that on S_ε, as $\varepsilon \to 0$, $Q \to P$ and $\sigma(P) \to \sigma(Q)$, we have

$$\lim_{\varepsilon\to 0} \iint\limits_{S_\varepsilon} \frac{\sigma(Q)}{\varepsilon}\mathrm{d}s(Q) = \sigma(P)\lim_{\varepsilon\to 0}\frac{1}{\varepsilon} \iint\limits_{S_\epsilon} \mathrm{d}s(Q) = \Theta\sigma(P)\lim_{\varepsilon\to 0} \varepsilon = 0,$$

$$\lim_{\varepsilon\to 0} \iint\limits_{S_\varepsilon} \frac{\sigma(Q)\vec{r}(P,Q)}{\varepsilon^3}\mathrm{d}s(Q) = \sigma(P)\lim_{\varepsilon\to 0}\frac{1}{\varepsilon^3} \iint\limits_{S_\epsilon} (\vec{r_P} - \vec{r_Q})\mathrm{d}s(Q) = \Theta\sigma(P)\lim_{\varepsilon\to 0} \frac{\vec{r_P} - \vec{r_c}}{\varepsilon}.$$

If we define

$$\vec{n_P} = \Theta \lim_{\varepsilon\to 0} \frac{\vec{r_c} - \vec{r_P}}{\varepsilon}, \tag{6}$$

then the formulae for evaluating the potential and velocity values at point P which is located on surface S are obtained as

$$\phi(P) = -\iint_S \frac{\sigma(Q)}{r(P,Q)} \mathrm{d}s(Q), \tag{7a}$$

$$\vec{v}(P) = -\sigma(P)\vec{n_P} + \iint_S \frac{\sigma(Q)\vec{r}(P,Q)}{r^3(P,Q)} \mathrm{d}s(Q), \tag{7b}$$

where $\iint_S \mathrm{d}s$ implies the Cauchy principal value of the surface integration.

The definition of $\vec{n_P}$ in Eq. (6) indicates that the direction of $\vec{n_P}$ is from point P to the gravity center of the surface area S_ε, which is a more general definition of normal vector valid even on non-smooth surfaces. On smooth surfaces, $\vec{n_P}$ is perpendicular to the surface everywhere, i.e. its direction is identical to the conventional normal vectors.

If $\vec{n_P}$ is calculated according to Eq. (6), the solid angle Θ and gravity center $\vec{r_c}$ must be evaluated. A simpler formula for $\vec{n_P}$ may be obtained if the following relation which is based on the fact that S_c and S_ε share the same boundary curve is used:

$$\int_{S_c}\!\!\int \vec{n}\,\mathrm{d}s = \int_{S_\varepsilon}\!\!\int \vec{n}\,\mathrm{d}s. \tag{8}$$

Since

$$\lim_{\varepsilon\to 0}\int_{S_\varepsilon}\!\!\int \frac{\sigma(Q)\vec{r}(P,Q)}{\varepsilon^3}\mathrm{d}s(Q) = -\sigma(P)\lim_{\varepsilon\to 0}\frac{1}{\varepsilon^2}\int_{S_\varepsilon}\!\!\int \vec{n}(Q)\mathrm{d}s(Q) = -\sigma(P)\lim_{\varepsilon\to 0}\frac{1}{\varepsilon^2}\int_{S_c}\!\!\int \vec{n}\,\mathrm{d}s,$$

another definition for $\vec{n_P}$ is given as

$$\vec{n_P} = \lim_{\varepsilon\to 0}\frac{1}{\varepsilon^2}\int_{S_c}\!\!\int \vec{n}\,\mathrm{d}s. \tag{9a}$$

In the above formulation, $\vec{n_P}$ can be obtained by integrating the unit normal distribution along the surrounding area of point P, i.e. S_c. One may take note that $\vec{n_P}$ is not a unit normal vector. From Eq. (9a), its value can be determined to vary from *0* to π. For example, $|\vec{n_P}| = 0$ when the solid angle subtended at P by the surface S is either *0* or 4π (this is the extreme case for the problem); $|\vec{n_P}| = \pi$ when surface S is locally smooth at point P. In the utilization of Eq. (9a), there is no necessity to consider solid angles and gravity centers. Further simplification for Eq. (9a) is still possible if S_c is constructed by N plane elements (see Fig. 3). It follows that Eq. (9a) can be simplified and written as

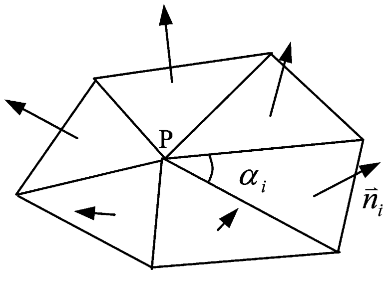

Fig. 3. Plane element discrete surface.

$$\vec{n}_P = \frac{1}{2}\sum_{i=1}^{N} \alpha_i \vec{n}_i. \tag{9b}$$

Here α_i is the angle subtended at point P in element i, and $\vec{n}_i$ is the unit normal vector on element i $(i = 1, 2, \ldots, N)$. Eq. (9b) is very easy to implement in numerical calculations. It is not the weighted average approximation of all unit normal vectors of its surrounding elements, but the exact direction of the self-induced velocity at point P if it is a node on a plane element discrete surface. Many other schemes proposed use of the weighted average to evaluate the normal vector at point P (purportedly) resulting in on equivalent or similar formulations to Eq. (9b). However, It should be noted that these other formulations are most likely come from approximation, and not the (natural) result of strict mathematical analysis. On the other hand, Eq. (9b) is mathematically exact.

2.2. Potential flow model

For large-scaled bubbles (say larger than millimeter) as considered in this paper, the effect of surface tension is insignificant during most of the bubble's lifetime and is thus neglected (see also [5]). For a general potential flow problem, there exists a potential function $\phi(x, y, z, t)$ in the fluid region bounded by some bubbles and solid structures. A rectangular coordinate system (x, y, z) is adopted with the z-axis pointing vertically upwards. Potential function ϕ is a harmonic function over the whole flow domain (see Fig. 4), i.e.

$$\nabla^2\phi = 0. \tag{10}$$

The kinematic and dynamic boundary conditions governing the motion of the bubble surface are

$$\frac{D\mathbf{x}}{Dt} = \nabla\phi, \tag{11a}$$

$$\frac{D\phi}{Dt} = 1 + \frac{1}{2}|\nabla\phi|^2 - \delta^2 z - \varepsilon\left(\frac{V_0}{V}\right)^{\lambda}, \tag{11b}$$

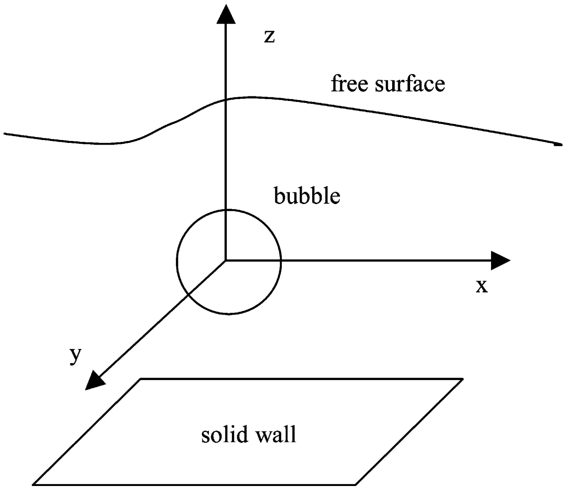

Fig. 4. Coordinate system.

where $\mathbf{x}$ denotes the spatial position of the fluid particle on bubble surface. Eq. (11b) results from the assumption that the gas inside the bubble is ideal and its motion is neglected, i.e. $p = p_c + p_0(V_0/V)^\lambda$, where P_c is the constant pressure of vapor; V is the volume of the bubble; V_0 and p_0 are the initial volume and pressure of the non-condensable gas, respectively; λ is the ratio of specific heat of the gas. In the formulations (11a), (11b), the length scale is non-dimensionalized by the maximum Rayleigh bubble radius R_m; and pressure is non-dimensionalized by pressure difference $\Delta p = p_\infty - p_c$, $\varepsilon = p_0/\Delta p$ and $\delta = \sqrt{\rho g R_\mathrm{m}/\Delta p}$ are non-dimensional parameters which characterize the strength (initial pressure) and buoyancy, respectively (see [14], for details).

When jet impact occurs and followed by the formation of toroidal shaped bubble, a vortex ring must be introduced to describe the rotational part of flow. The total potential ϕ is decomposed into two parts: a potential associated with the circulation generated by the impact, $\bar{\psi}$, termed the ring potential, and a remainder, φ which is smooth in the entire fluid domain. The ring potential at any point P in the flow field or the bubble surface can be efficiently obtained by

$$\bar{\psi}(P) = \frac{\Gamma\Theta(P)}{4\pi}, \tag{12}$$

where Θ is the solid angle subtended at the point P by the vortex ring; the strength of the vortex ring Γ can be determined by the difference of potential values at the impact point. Γ is kept as a constant value (i.e. not changing with time) once the impact occurred. The location of vortex ring can stay invariant as long as it lies within the toroidal bubble, and hence $\bar{\psi}$ will not change with time. (Only when there is substantial subsequent movement of the toroidal bubble, then the vortex ring is moved to a new location still within the torus and $\bar{\psi}$ changes accordingly.) It may be noted that based on an alternative approach by Best [1], the "physical" vortex sheet is located in front of the jet tip and convected with the fluid flow. The shape of the vortex sheet can subsequently be highly stretched and complicated. In the ideal fluid model of this work and Best, the vortex sheet only provides a circulation flow and separates the potential jump across it. If one discounts the exact location of the potential jump (potential is not a physical parameter anyway), it is possible to replace the more complex so-called "real" vortex sheet with a "fake", but much simpler, representation. The vortex ring introduced in the present paper is a simplified model of the "real" vortex sheet and it provides the same amount of circulation flow. The remainder potential φ should also satisfy the Laplacian equation (10), but with the following modified boundary conditions:

$$\frac{D\mathbf{x}}{Dt} = \nabla\varphi + \nabla\bar{\psi}, \tag{13a}$$

$$\frac{D\varphi}{Dt} = -\nabla\bar{\psi}\cdot(\nabla\varphi + \nabla\bar{\psi}) + 1 + \frac{1}{2}\left|\nabla\varphi + \nabla\bar{\psi}\right|^2 - \delta^2 z - \varepsilon\left(\frac{V_0}{V}\right)^\lambda. \tag{13b}$$

One may refer to [20] for more details.

3. Numerical implementation

To solve Eqs. (7a), (7b) numerically, the surface S is discretized into a set of M nodal points P_i $(i = 1, \ldots, M)$, and N triangular elements Δ_j $(j = 1, \ldots, N)$. The source distribution σ on each element is assumed to vary linearly, and a set of M global base functions are defined as follows:

$$\psi_i = \begin{cases} 1 & \text{on node } P_i, \\ 0 & \text{on other nodes} \quad (i = 1, \ldots, M), \\ \text{linear interpolation} & \text{on each element.} \end{cases} \tag{14}$$

After substitution of the above formulae, Eq. (7a) in its discrete form can be written as

$$\phi_i = -\sum_{k=1}^{M} \sigma_k \left[\sum_{j=1}^{N} \oiint_{\Delta_j} \frac{\psi_k(Q)}{r_i(Q)} \mathrm{d}s(Q) \right]. \tag{15}$$

Here $\vec{r_i}(Q)$ is the vector from Q on Δ_j to P_i $(i = 1, \ldots, M)$. The portions enclosed by the square brackets in Eq. (15) are only dependent on the geometry of the problem. All integration in Eq. (15) can be carried out using the analytical formulae listed in Appendix A.

In order to analytically evaluate the induced velocity of any control point by the linear source distribution over any triangular element, one can start and transform Eq. (3b) into a suitable form. Fig. 5 illustrates the local coordinate system used in the analysis. The induced velocity can be derived by applying the ∇_P operator to the induced potential (Eq. (3a)) directly, i.e.

$$\vec{v}(P) = -\nabla_P \iint_S \frac{\sigma(Q)}{r(P,Q)} \mathrm{d}s(Q) = \iint_S \sigma(Q) \nabla_Q \left[\frac{1}{r(P,Q)} \right] \mathrm{d}s(Q). \tag{16a}$$

Since $\nabla_Q = \tilde{\nabla}_Q + \vec{n_Q}(\partial/\partial n_Q)$, therefore

$$\begin{aligned} \vec{v}(P) &= \iint_S \tilde{\nabla}_Q \frac{\sigma(Q)}{r(P,Q)} \mathrm{d}s(Q) - \iint_S \frac{\tilde{\nabla}_Q \sigma(Q)}{r(P,Q)} \mathrm{d}s(Q) + \iint_S \sigma(Q) \frac{\partial}{\partial n_Q} \left[\frac{1}{r(P,Q)} \right] \vec{n_Q} \mathrm{d}s(Q) \\ &= \oint_{\Gamma_e} \frac{\sigma(Q)}{r(P,Q)} \vec{n_s}(Q) \mathrm{d}\Gamma(Q) - \iint_S \frac{\tilde{\nabla}_Q \sigma(Q)}{r(P,Q)} \mathrm{d}s(Q) + \iint_S \sigma(Q) \frac{\partial}{\partial n_Q} \left[\frac{1}{r(P,Q)} \right] \vec{n_Q} \mathrm{d}s(Q). \end{aligned} \tag{16b}$$

Here the operators ∇_P and ∇_Q are only applied to the control point P and source point Q, respectively; $\tilde{\nabla}$ is the projection of operator ∇ on the triangular element which is bounded by the edges Γ_e; $\vec{n_s}$ is the unit vector perpendicular to the respective edge and on the same plane as the triangular element. If the control point P is located on the triangular element, then the first term in Eq. (7b) must be added to Eq. (16) to become

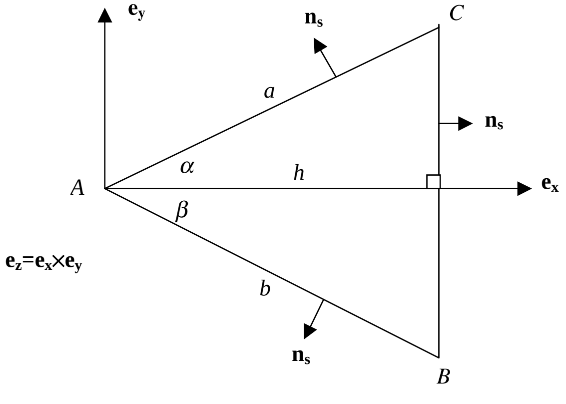

Fig. 5. Analytical integral of the potential and velocity induced by a linear source distribution over any triangular element.

$$\vec{v}(P) = -\,\sigma(P)\vec{n}_p + \oint_{\Gamma} \frac{\sigma(Q)}{r(P,Q)}\vec{n}_s(Q)\,\mathrm{d}\Gamma(Q) + \iint\limits_{S} \sigma(Q)\frac{\partial}{\partial n_Q}\left[\frac{1}{r(P,Q)}\right]\vec{n}_Q\,\mathrm{d}s(Q) - \iint\limits_{S} \frac{\tilde{\nabla}_Q\sigma(Q)}{r(P,Q)}\mathrm{d}s(Q). \tag{17}$$

After substitution of the discretized source distribution $\sigma(Q) = \sum_{k=1}^{M}\sigma_k\psi_k(Q)$, Eq. (17) is further transformed as follows:

$$\vec{v}_i = -\sigma_i\vec{n}_{Pi} + \sum_{k=1}^{M}\sigma_k\left[\sum_{j=1}^{N}\oint_{\Gamma_j}\frac{\psi_k(Q)}{r_i(Q)}\vec{n}_s(Q)\,\mathrm{d}\Gamma(Q)\right] + \sum_{k=1}^{M}\sigma_k\left[\sum_{j=1}^{N}\iint\limits_{\Delta_j}\frac{\psi_k(Q)\vec{r}_i(Q)\cdot\vec{n}_j}{r_i^3(Q)}\vec{n}_j\,\mathrm{d}s(Q)\right] - \sum_{k=1}^{M}\sigma_k\left[\sum_{j=1}^{N}\iint\limits_{\Delta_j}\frac{\tilde{\nabla}_{(Q)}\psi_k(Q)}{r_i(Q)}\mathrm{d}s(Q)\right]. \tag{18}$$

One may note that, all integrations in Eq. (18) can be evaluated exactly by the analytical formulae which are listed in Appendix A. By defining

$$A_{ik} = -\sum_{j=1}^{N}\oiint_{\Delta_j}\frac{\psi_k(Q)}{r_i(Q)}\mathrm{d}s(Q), \tag{19a}$$

$$B_ik = \sum_{j=1}^{N}\oiint_{\Delta_j}\left[\frac{\psi_k(Q)\vec{r}_i(Q)\cdot\vec{n}_j}{r_i^3(Q)}\vec{n}_j - \frac{\tilde{\nabla}_Q\psi_k(Q)}{r_i}\right]\mathrm{d}s(Q) + \sum_{k=1}^{M}\frac{\psi_k(Q)}{r_i(Q)}\vec{n}_s(Q)\,\mathrm{d}\Gamma(Q), \tag{19b}$$

we can obtain two matrix expressions of ϕ_i and $\vec{v}_i$ as

$$\phi_i = \sum_{k=1}^{M}A_{ik}\sigma_k, \tag{20a}$$

$$\vec{v}_i = -\sigma_i\vec{n}_{P_i} + \sum_{k=1}^{M}\vec{B_ik}\sigma_k. \tag{20b}$$

In this approach, there is no need of interpolation to approximate the velocities and normal vectors on each node.

At a given time step, if the potential on the boundaries (like on the bubble(s) and free surface) is given, Eq. (20a) is used to compute for the unknown σ. The velocity on surfaces is then obtained from Eq. (20b). From there, Eqs. (11a) and (11b) are used to update for the next time step, and the sequence of calculation continues. For problems where there is the presence of rigid surface(s) and the normal velocity is known, a combination of Eqs. (20a) and (20b) are used to evaluate for σ, to be followed by the calculation of the unknown potential and velocity on the rest of the boundaries. As before, Eqs. (11a) and (11b) are employed to evolve for the next time step.

In the simulation of bubble dynamics with jet formation, the jet tip exhibits strong sink characteristic. The elements on the bubble surface tend to converge fairly rapidly towards the jet tip and quickly become over crowded in the jet tip vicinity. (Strictly, the inherent presence of more elements for better resolution of the jet is a reasonable and acceptable development. The objection arises when too many elements are in the

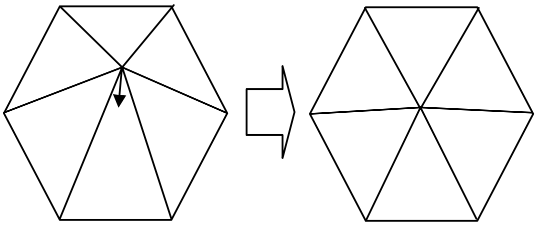

Fig. 6. EMT mesh optimization.

jet tip vicinity which has the consequence of thinning out the element distribution in other regions.) This accumulated imbalance of element distribution will eventually result in the early breakdown of the simulation in the absence of other interventions. In order to make the element distribution as reasonably uniform as possible, EMT is introduced. EMT is based on the idea that if the mesh is made of elastic ribbons, it should be able to automatically adjust its shape optimally: all segment lengths are close to equal. In essence, the optimum mesh is found by minimizing the total elastic energy stored in each segment of the mesh. This approach has an advantage that it actively seeks in a forward manner the optimum mesh for computation at each time step. This is quite different from those where the re-distribution takes place after the calculations are made. Compared with the conventional node insertion and deletion approach, EMT keeps the number of nodes and topological structure of the mesh unchanged. (This may become a critical issue in deriving an efficient algorithm for matrix inversion in the simulation of multiple bubbles with complex geometric and yet the number of elements is kept constant without the additional complexities of mesh refinement and deletion.) Instead of advancing by the material velocity, EMT produces an optimum mesh shifting velocity, which ensures the regularity of the mesh after advancement (see Fig. 6).

It is found [13] that EMT has enabled a much more even distribution of the meshes representing the bubble surface even in the midst of a strong jet formation where there is great difference in the surface velocity of the bubble. In doing so, the incorporation of EMT has permitted the use of significantly larger time stepping and still within reasonable accuracy.

A Bi-CG iterative solver is implemented to solve the resulting linear system. Bi-CG iterative solver is a member of conjugate gradient (CG) iterative solver family. CG solver is most efficient in solving symmetric positive-definite linear systems, while unfortunately the present resulting system is not symmetric positive-definite. Since Bi-CG solver is a little less efficient than CG solver but can solve any linear systems, it seems a logical choice to implement the Bi-CG solver. It is found that the Bi-CG solver is far more efficient than the direct solver based on Gaussian elimination and accelerates the simulation greatly. In addition, the Bi-CG solver has another advantage over the direct solver in that it can easily control the solution error. In our calculations, the convergence condition is set at 10^{-10}. (The typical CPU time to simulate the evolution of explosion bubble(s) range from much less than 1 h for a single Rayleigh bubble in one period to about 5 h for the more complex two bubbles in the presence of the free surface running on a Pentium III 1.2 GHz PC with 1 GB RAM; see below.)

4. Numerical results and discussions

One of the simplest bubble dynamics problems is the Rayleigh bubble. There exists a simple ordinary differential equation (ODE) describing its behavior, which can be solved accurately by standard ODE solver such as the fourth-order Runge–Kutta method. The Rayleigh bubble calculated here has initial radius $R_0 = 0.1651$ and pressure $\varepsilon = 100$ and $\delta = 0$. The initial spherical bubble surface is discretized into

1280 triangular elements using a projection and refinement method starting from a regular icosaedron. Since in this case the bubble is expanding and collapsing uniformly and so is the mesh distribution kept uniform, no mesh optimization via EMT is applied. Fig. 7(a) shows the computed radius variation over two expanding and collapsing cycles' evolution of Rayleigh bubble; this compares very well with the direct solution of Rayleigh equation (depicted as solid line in the same figure). Fourth-order Runge–Kutta time marching scheme is used in both the simulation and solution of the Rayleigh's equation. Theoretically, Rayleigh bubble will keep to the spherical shape characteristic throughout its whole lifetime, i.e. the radius at all surface points should be identical. In order to evaluate the influence of numerical errors on the de-

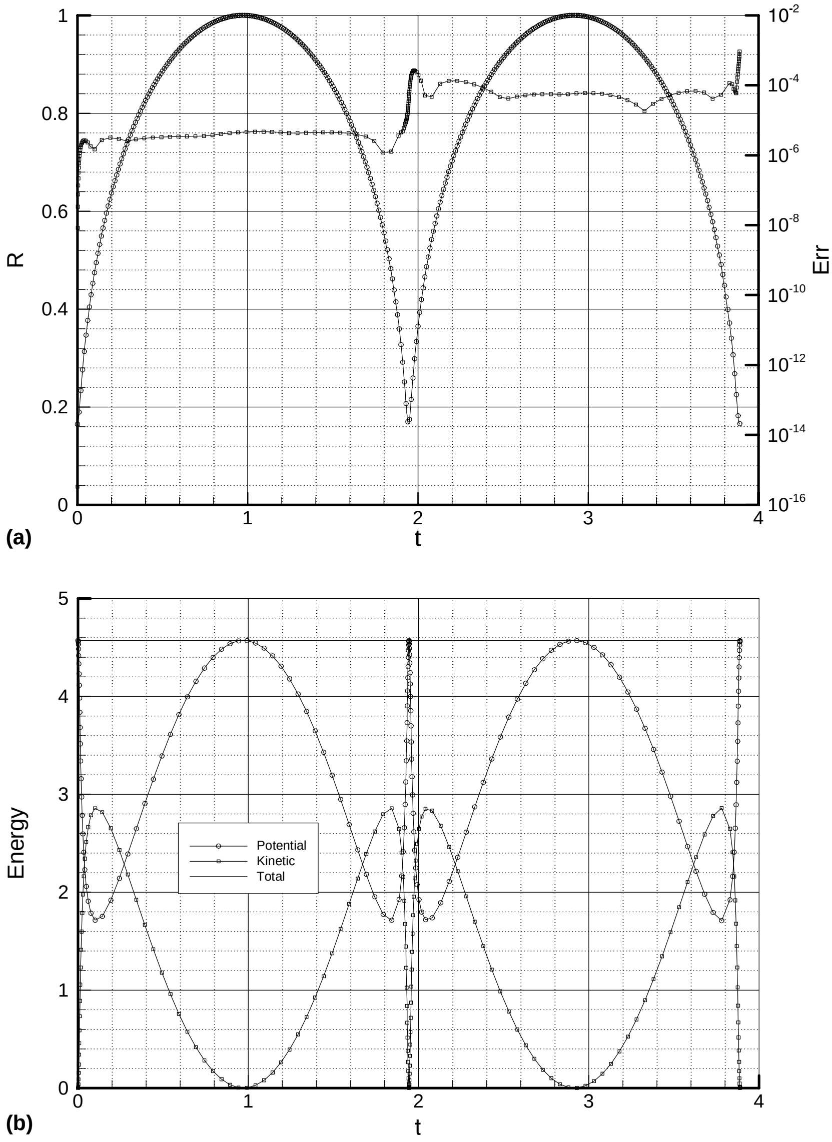

Fig. 7. (a) Radius variation and error accumulation of the Rayleigh bubble with $\varepsilon = 100$ and $R_0 = 0.1651$. (b) Energy balance of the Rayleigh bubble with $\varepsilon = 100$ and $R_0 = 0.1651$.

formation of the Rayleigh bubble, the *maximum* absolute deviation of the bubble surface from the spherical Rayleigh's bubble is also shown in Fig. 7(a). The error increases when the bubble is near the minimum size point and is relatively flat otherwise. This may imply that the Rayleigh bubble is most unstable at its minimum size. Generally, the error line indicates a mild increasing trend as the numerical errors are constantly accumulating during the computations. The energy balance of the Rayleigh bubble is shown next in Fig. 7(b). The non-dimensional kinetic energy of the bubble sphere is evaluated as

$$E_k = \frac{1}{2}\int_S \phi \frac{\partial \phi}{\partial n}\,\mathrm{d}s, \tag{21a}$$

while the potential energy counterpart (which is a combination of the gravitational potential energy and the internal potential energy) is given as

$$E_p = V\left(1 - \delta^2 z_c\right) + \frac{\varepsilon V}{\lambda - 1}\left(\frac{V_0}{V}\right)^{\lambda} \tag{21b}$$

(see also [20]). Here z_c is the depth of the bubble center. The total energy $E = E_k + E_p$ is a constant due to the law of energy conservation. In Fig. 7(b) the solid line with circular markers is the potential energy which includes the bubble and fluid potentials, while the solid line with square markers denotes the kinetic energy. The total energy comprising the sum of the potential and kinetic energy assumes an almost perfect constant quantity over the whole evolution of the Rayleigh bubble even at the most unstable point of minimum bubble size. (It may just be noted that when the DBEM of [18] is utilized to make an identical run, the results obtained are fairly similar with the same level of accuracy compared to the analytical solution.)

In the next case the gravity effect is added into the Rayleigh bubble to study the evolution of an explosion bubble in the gravity field. All parameters are set equal to the Rayleigh bubble case ($R_0 = 0.1651$ and $\varepsilon = 100$) except the gravity is set as $\delta^2 = 0.05$. The initial spherical bubble is also discretized into 1280 triangular elements. The evolution of the bubble is shown in Fig. 8(a). Fig. 8a(1) indicates the initial bubble. (The color contour represents the magnitude of the potential function.) During the expanding phase gravity shows little influence on the bubble behavior. When the bubble reaches its maximum size, it is still kept nearly spherical as depicted in Fig. 8a(2). In the consequent collapsing phase, the effect of gravity is felt. The lower bubble boundary moves faster than the upper one which makes the bubble becomes a bean-like shape at non-dimensional time of $t = 1.679$ and the start of jet formation process (Fig. 8a(3)). In Fig. 8a(4) the jet is fully developed and going to impact the upper boundary of the bubble. At the dimensionless time of 1.700 (Fig. 8a(5)), the jet has impacted on the opposite bubble surface and a toroidal bubble is formed via the employment of a surgical-cut and a vortex ring. The purple bar inside the toroidal bubble is the vortex ring placed to simulate the rotational part of the flow. Fig. 8a(6) shows the further evolution of the toroidal bubble which is in the process of rebounding.

Next, to study the effects of increase of gravity on the bubble behavior, the gravity parameter δ^2 is increased to 0.25 and the simulation is repeated with the same initial conditions. The results are shown in Fig. 8(b). It is difficult to detect the influence of gravity on the bubble growth/expansion phase and the bubble shape at its maximum size (Fig. 8b(2)) is almost identical to the one shown in Fig. 8a(2), except that the vertical position of the bubble center for the latter is lower. In the ensuing collapsing phase, the influence of gravity is discernible. The larger gravity of $\delta^2 = 0.25$ accelerates the deformation of the bubble, which brings the starting point of jet formation forward to as early as $t = 1.558$ when the bubble is still relatively large in dimension (compare Fig. 8a(3) and b(3)). What is interesting to note is that the total time taken for the jet to be fully developed as indicated by the pending formulation of the toroidal shaped bubble is not greatly affected by the increased gravity. The increased gravity only results in the larger volume of the bubble in the final stage of collapse. Fig. 8b(5) at $t = 1.914$ shows that the (bubble) jet is closed to make impact on the top surface of the bubble which then lead to the formation of the toroidal

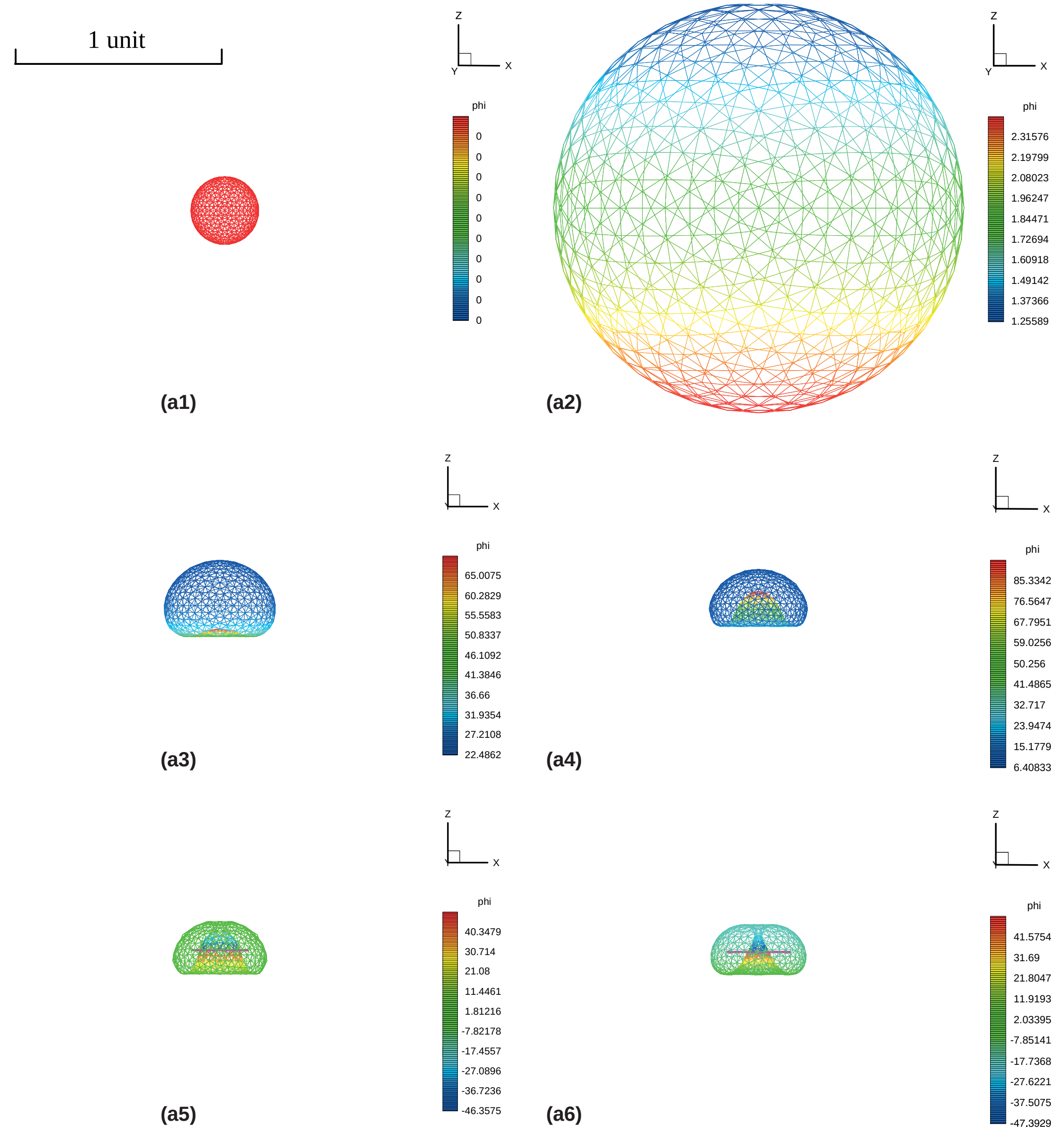

Fig. 8. a(1) Explosion bubble ($\varepsilon = 100$, $\delta^2 = 0.05$ and $t = 0.000$). a(2) Explosion bubble ($\varepsilon = 100$, $\delta^2 = 0.05$ and $t = 0.905$). a(3) Explosion bubble ($\varepsilon = 100$, $\delta^2 = 0.05$ and $t = 1.679$). a(4) Explosion bubble ($\varepsilon = 100$, $\delta^2 = 0.05$ and $t = 1.694$). a(5) Explosion bubble ($\varepsilon = 100$, $\delta^2 = 0.05$ and $t = 1.700$). a(6) Explosion bubble ($\varepsilon = 100$, $\delta^2 = 0.05$ and $t = 1.705$). b(1) Explosion bubble ($\varepsilon = 100$, $\delta^2 = 0.25$ and $t = 0.000$). b(2) Explosion bubble ($\varepsilon = 100$, $\delta^2 = 0.25$ and $t = 0.903$). b(3) Explosion bubble ($\varepsilon = 100$, $\delta^2 = 0.25$ and $t = 1.558$). b(4) Explosion bubble ($\varepsilon = 100$, $\delta^2 = 0.25$ and $t = 1.869$). b(5) Explosion bubble ($\varepsilon = 100$, $\delta^2 = 0.25$ and $t = 1.914$). b(6) Explosion bubble ($\varepsilon = 100$, $\delta^2 = 0.25$ and $t = 2.054$). (c) Gravity center trajectories of an explosion bubble in different gravity field ($\varepsilon = 100$). (d) Energy balance of an explosion bubble in different gravity field ($\varepsilon = 100$).

shape. The toroidal bubble once formed continues to evolve and subsequently contract in volume to reach its minimum size at time $t = 2.054$ (Fig. 8b(6)). Rebounding follows subsequently. It can be suggested that the gravity strength determines the bubble size at the jet impact. It may be noted that EMT was applied in

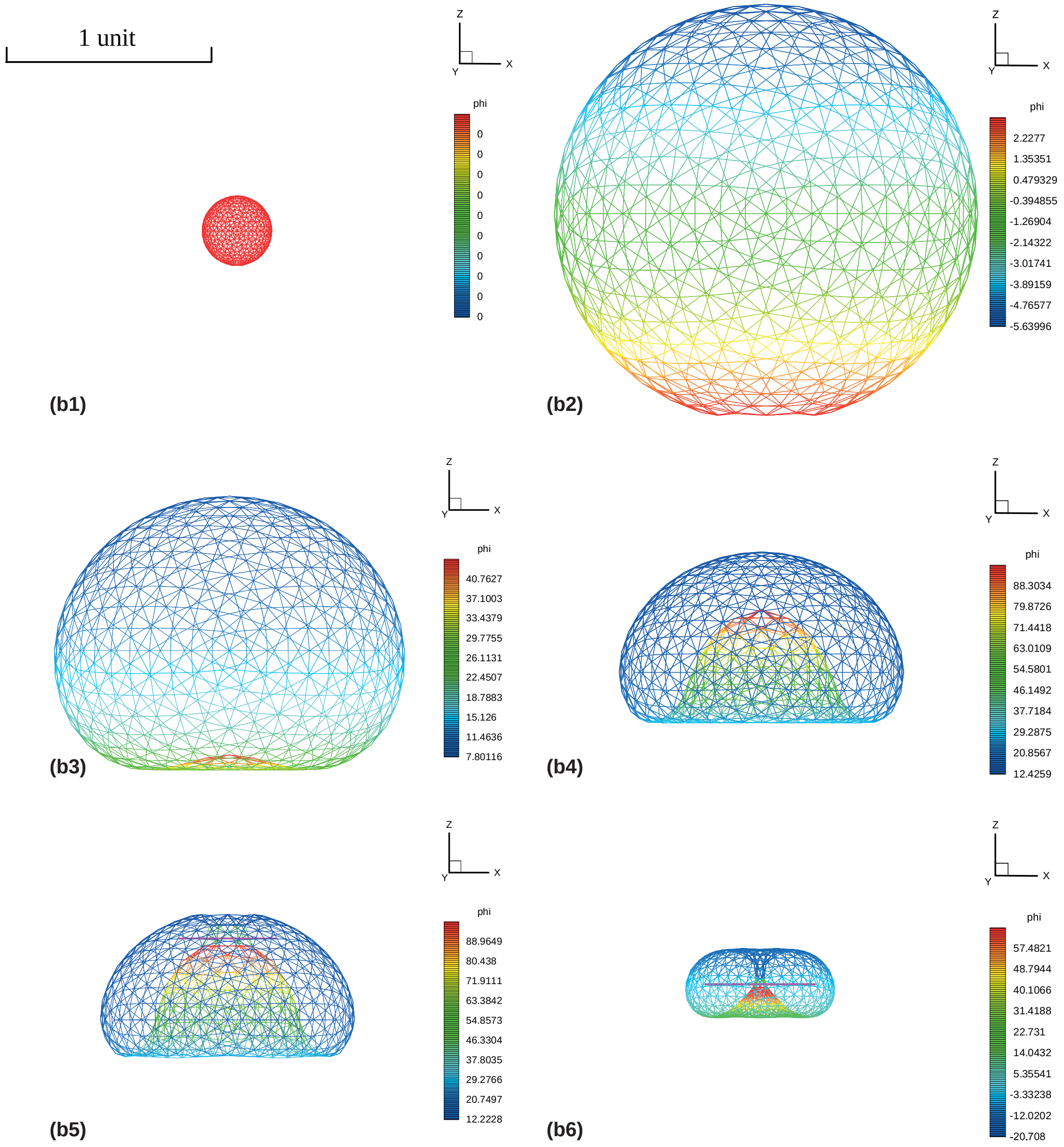

Fig. 8. (*continued*)

both the simulations of Figs. 8(a) and (b) which serves to avoid the overcrowding of elements in the jet tip vicinity. EMT works well throughout the phase of the toroidal bubble evolution. Had EMT not been employed, there would have been necessary to employ nodes insertion to avoid exceedingly large size elements and mesh refinements at other parts so that the shape of the bubble is still reasonably ‘smoothed’. Fig. 8(c) compares the bubble (gravity) center rising trajectories in the different gravity field. It is as expected, the larger gravity case has a faster rise. For the bubble under smaller gravity effect, the rising speed

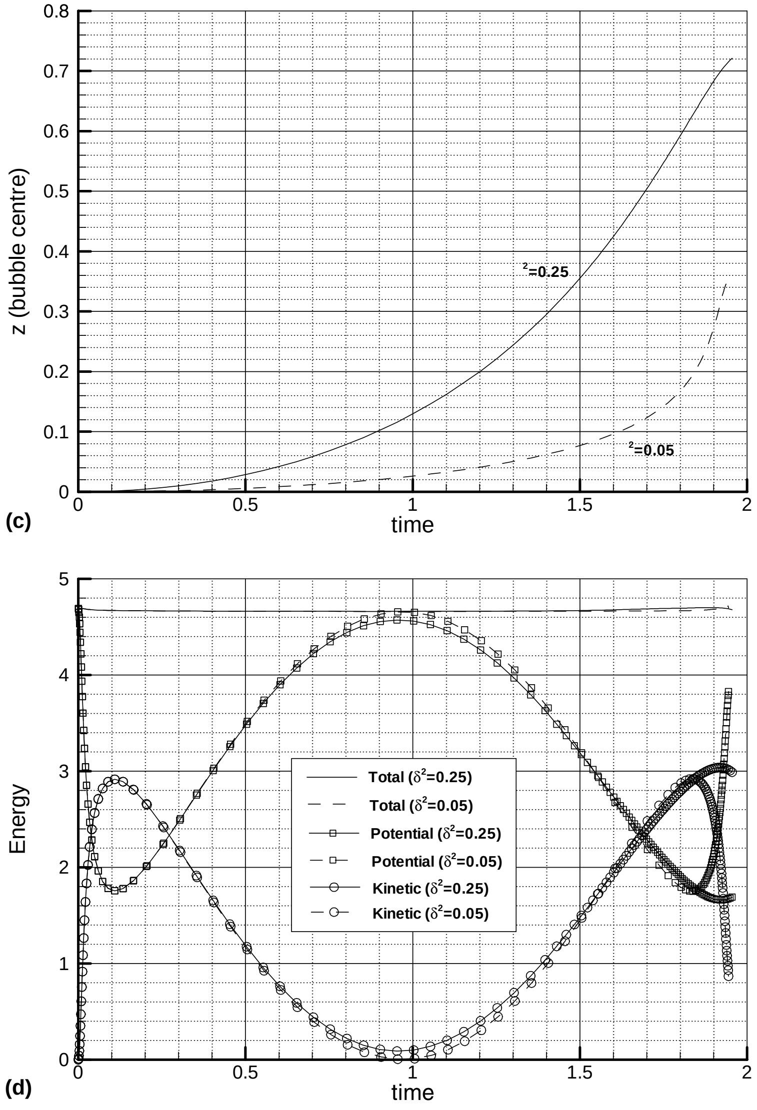

Fig. 8. (*continued*)

keeps to relatively low magnitude during most part of the evolution cycle, but it increases fairly rapidly towards the end of the collapsing phase. However, the change of rising speed is much less obvious for the bubble under the larger gravity influence. The energy balance (and its components) is shown in Fig. 8(d) for the respective δ^2. It can be observed that the total energy is maintained throughout, and the difference in δ^2 has resulted in different magnitude of the potential and kinetic energy.

In the next case the interaction between two symmetric explosion bubbles is studied. Buoyancy is set to zero ($\delta^2 = 0$). All other parameters are set equal to the Rayleigh bubble case $R_0 = 0.1651$ and initial pressure ($\varepsilon = 100$). The initial distance between the two bubbles is set to 1.5 dimensionless units. Each initial bubble surface is triangular discretized into 1280 elements. Fig. 9a(1) shows the initial state at $t = 0$. There is a symmetric expansion of the two bubbles with the outer-side boundaries moving faster compared

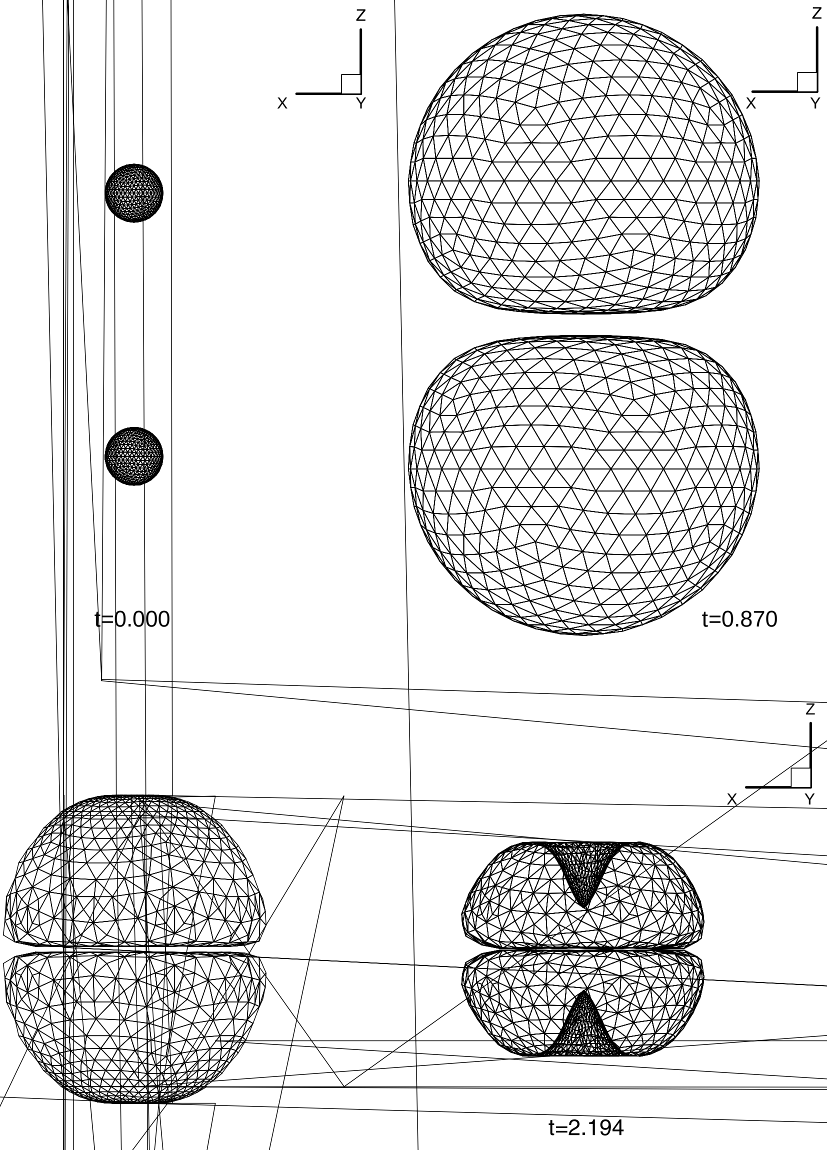

to the inner-side boundaries as constrained by the presence of the other bubble. With time, each bubble evolves into a bun-shaped as shown in Fig. 9a(2). Upon reaching the maximum volume at $t = 0.870$, the collapsing phase begins. The outer-side boundaries of each bubble stop its movement outwards and begin to move inwards while the inner-side boundaries continue to move outwards albeit at a much slower rate towards the inner-boundaries of the other bubble. With the outer-side boundaries of the two bubbles moving towards the symmetric plane, the jets at the outer-side boundaries start to develop which are shown in Fig. 9a(3). Fig. 9a(4) shows almost the full development of the associated jets which are going to impact the inner-side boundaries of the bubbles. Fig. 9(b) shows the energy balance of the evolution of one of the

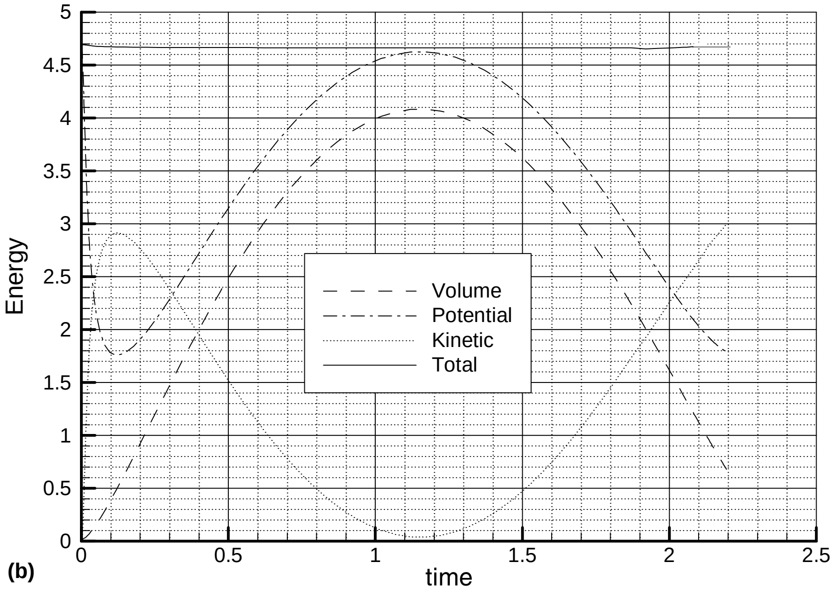

Fig. 9. (*continued*)

two symmetric bubbles. In fact, the volume, potential energy, kinetic energy and total energy of each bubble is almost identical to the other thereby further attesting to the accuracy of the assembled computer code. The total energy (the solid line in the figure) is almost constant throughout the bubble evolution.

In the forth case, both the gravity and free surface effects are taken into account, which form a complete three-dimension problem. Two bubbles with the same initial size and pressure ($R_0 = 0.1651$ and pressure $\varepsilon = 100$) are separated by the horizontal distance of 2 dimensionless units, and located 1.5 dimensionless units under the initially quiescent free surface. The gravity is in the vertical direction with strength $\delta^2 = 0.25$. Each initial bubble is still discretized into 1280 triangular elements, while the free surface with a non-dimensional size of 10×5 units is discretized into 1152 elements. The source distribution outside the surface mesh area is assumed to be null value. (Computations have been carried out with even larger extent and more elements on the free surface and the results differ by much less than 1% (not shown).) Fig. 10(1) shows the initial configuration. (On these figures, the color contour represents the magnitude of the potential function, ϕ.) At time $t = 0.122$ the bubbles are in their expanding phase and there can be found a small rise on the free surface (Fig. 10(2)). The maximum bubble size is reached when $t = 0.658$ which is displayed in Fig. 10(3). Some deformation of the bubble shape can be observed at this time. On the free surface, a higher rise is achieved and obvious surface peaks attributing to the presence of the two bubbles are observed. After reaching their maximum size, the two bubbles start to collapse and eventually leading to jet formation. At time $t = 1.338$, the oblique jets are formed, which are shown in Fig. 10(4). Correspondingly, there are two jets on the free surface pointing upwards.

The fifth case studies the evolution of one explosion bubble near a rigid spherical ball (see Fig. 11(1)) in the presence of the free surface. The explosion bubble is originally spherical with $R_0 = 0.1651$ and pressure $\varepsilon = 100$ and $\delta^2 = 0.25$. The radius of the rigid ball is one dimensionless unit and is located to the right side of the bubble at a distance of 2 dimensionless units. The initial free-surface is located 1.1 units above the bubble center. The initial bubble and rigid ball are still discretized into 1280 triangular elements, respectively, while the free surface is discretized into 1152 elements. At time 0.05666, the bubble is expanding spherically but the pressure inside the bubble is much lower than the initial state. The free-surface shows a marginal rise (see Fig. 11(2)). The color contour in Fig. 11 represents the pressure distribution. One may note the pressure distribution on the rigid ball due to the expanding gaseous bubble. The surface on the rigid ball nearest the bubble exhibits the largest magnitude of pressure exerted. The bubble continues to expand till its maximum size at time 0.8468 in Fig. 11(3). One can easily detect the asymmetrical shape of the bubble with the surface facing the rigid ball exhibiting a flatter feature compared to the diametrically opposite side of the bubble surface on the left. There is an obvious rise of the free surface due to the expanding bubble. On closer scrutiny, for the free surface in the vicinity and nearest the top section of the rigid ball, there is a slight depression of the surface compared to the initial quiescent state. One may note that in the "rushing" in of the fluid from the surrounding due to the rise of the free surface next to the

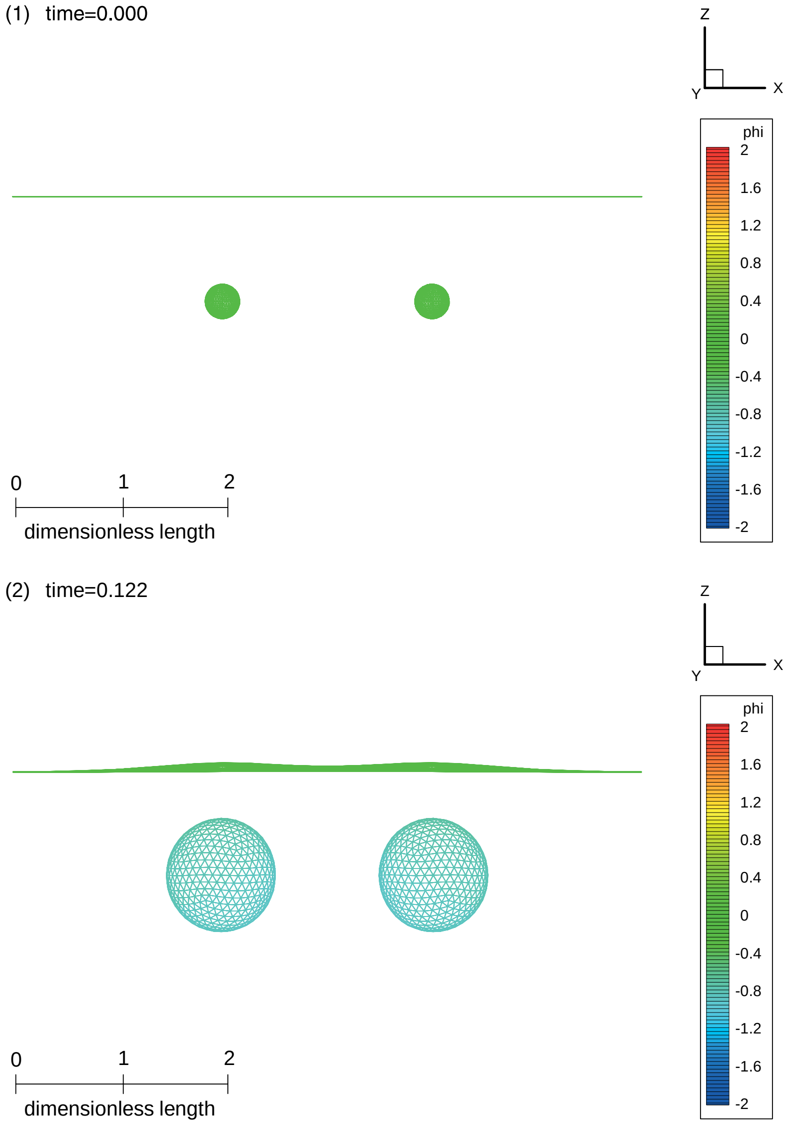

Fig. 10. Evolution of two bubbles near a free surface ($\varepsilon = 100$ and $\delta^2 = 0.25$). Time (1) 0.000, (2) 0.122, (3) 0.658 and (4) 1.338.

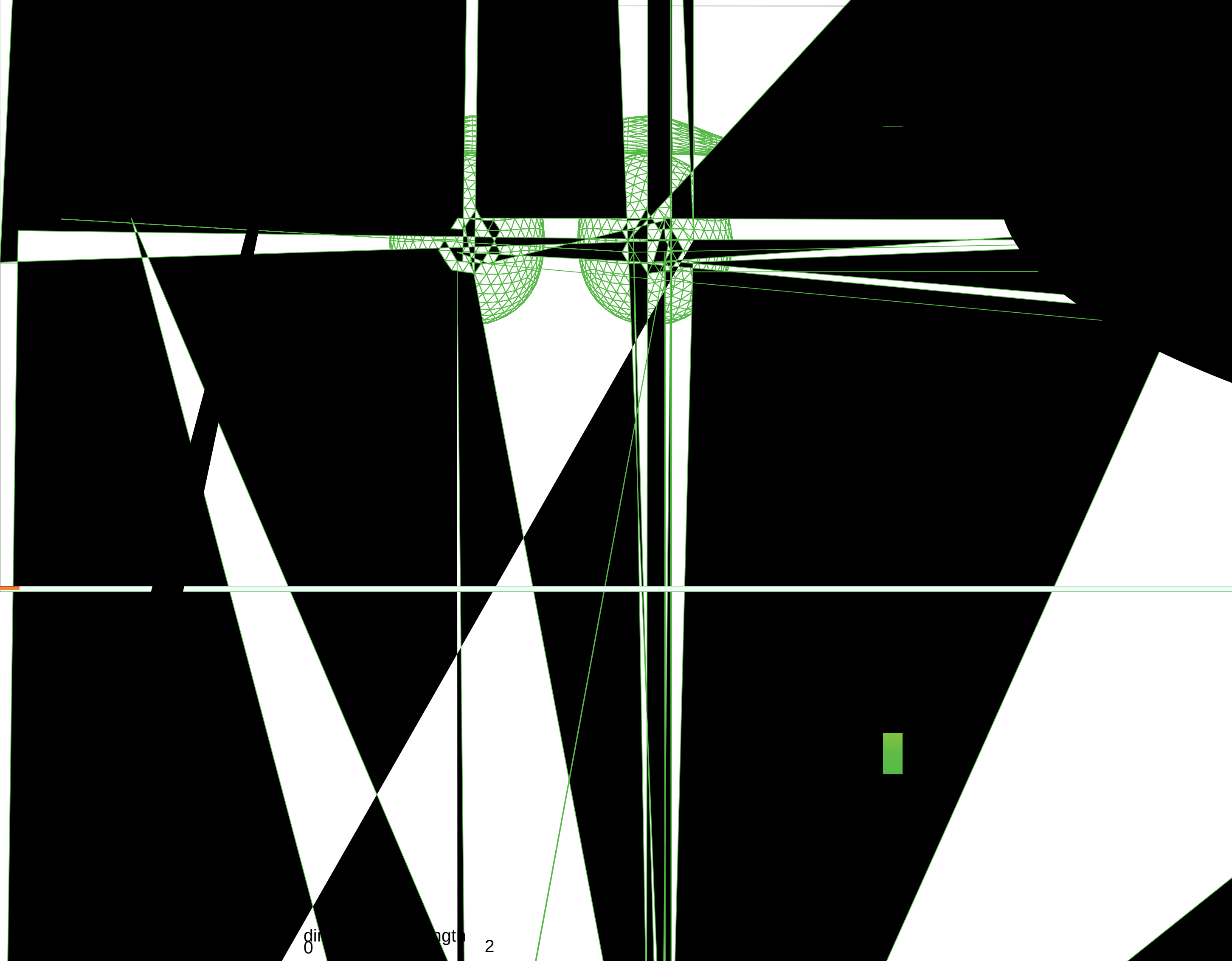

g bubble, the narr t een the rigid y
velocity region with a n ow pressure aused th
sphere pressure to move va eit marginal gresses.
a jet pointing downward ev during the nase.
veloped which is clearly obs i (4). The p ne i
xerted on the left side of the b the bubbl
becomes even higher although at has beco na

The presence of free surface, gravity effect and even the symmetric placement of bubble can give rise to jet(s) formation during the bubble(s) evolution. It is interesting to note their characteristics and differences. The free surface induced jet always points downwards, while the gravity induced jet always points upward and is not as sharp as the jet due to another bubble. For the bubble induced jet, it is always pointing towards the other bubble. Gravity effect also shows little influence during the expanding phase while the symmetric placement of bubbles indicates stronger influence during this stage of the bubble development.

In the sixth and final case using the present IBEM approach, a comparison is made between the simulation and the experimental data from Boyce and Debono [7]. To be described very briefly, the experiment

(1) time=0.000

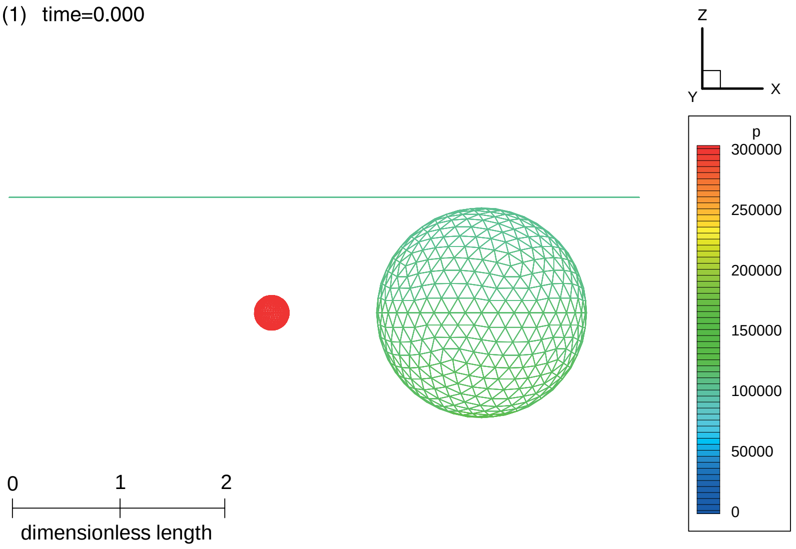

(2) time=0.0566597

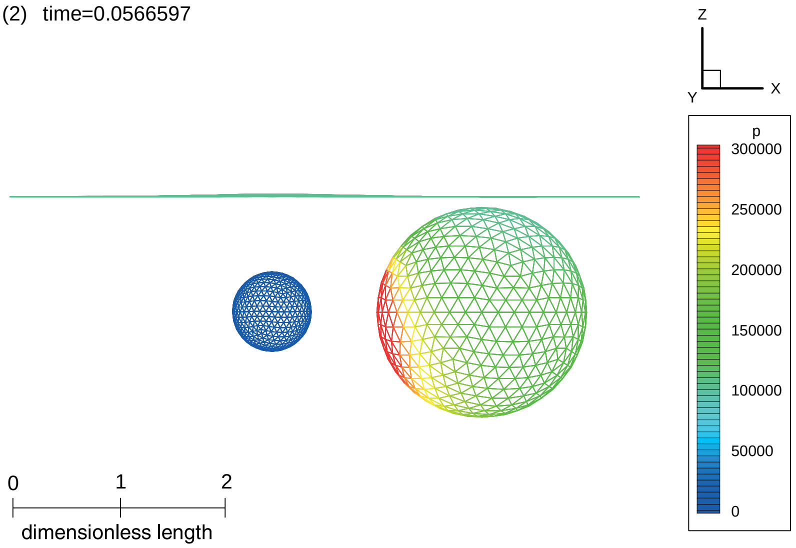

Fig. 11. Evolution of one bubble near a rigid ball under free surface ($\varepsilon = 100$ and $\delta^2 = 0.25$). Time (1) 0.000, (2) 0.0566597, (3) 0.846799 and (4) 1.44911.

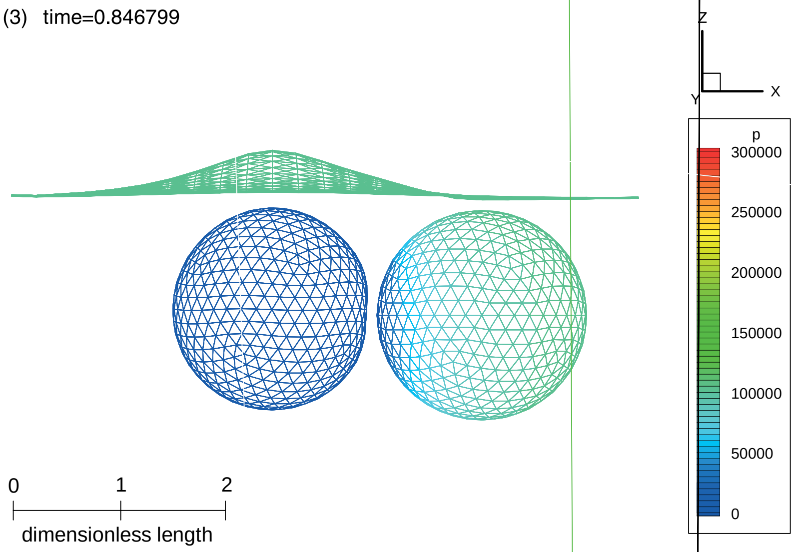

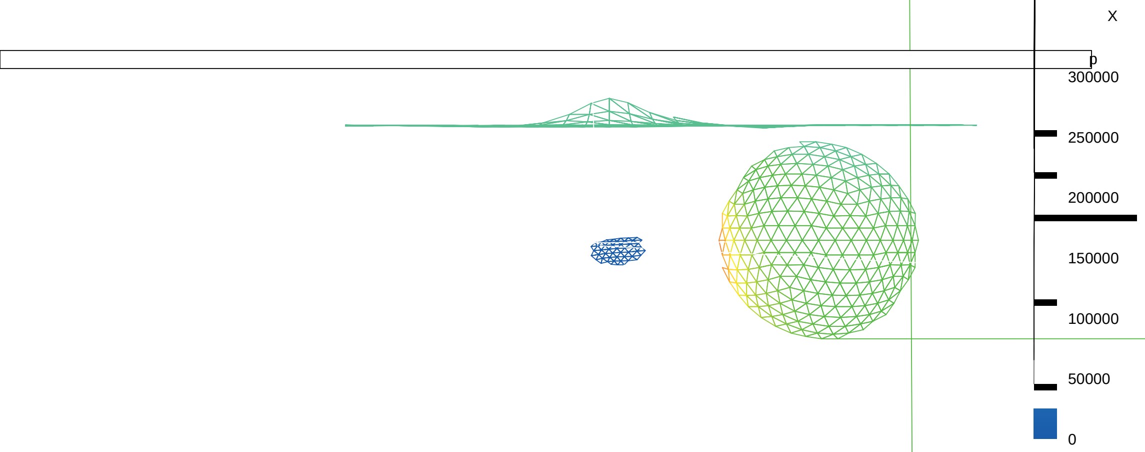

of an underwater explosion was carried out in an outdoor pond measuring about 18 m in diameter with an average depth of 7 m. An explosive charge of 55 g of Hexocire was placed and located at 3.5 m beneath the water surface at the center of the pond. A solid steel plate of thickness 0.2 m measuring 1.5 × 1.5 m was vertically placed 0.4 m away from the explosive charge (Fig. 12(a)). The charge detonation was synchronised with the very high speed video camera capable of recording up to 1000 frames per second to track the evolution of the bubble in the presence of the nearby steel plate. For the numerical simulation, the initial bubble radius R_0 and the initial bubble pressure P_0 is estimated based on the weight W (in kg) and the depth H (in meter) of the explosive by an empirical formula (see [15]) given as

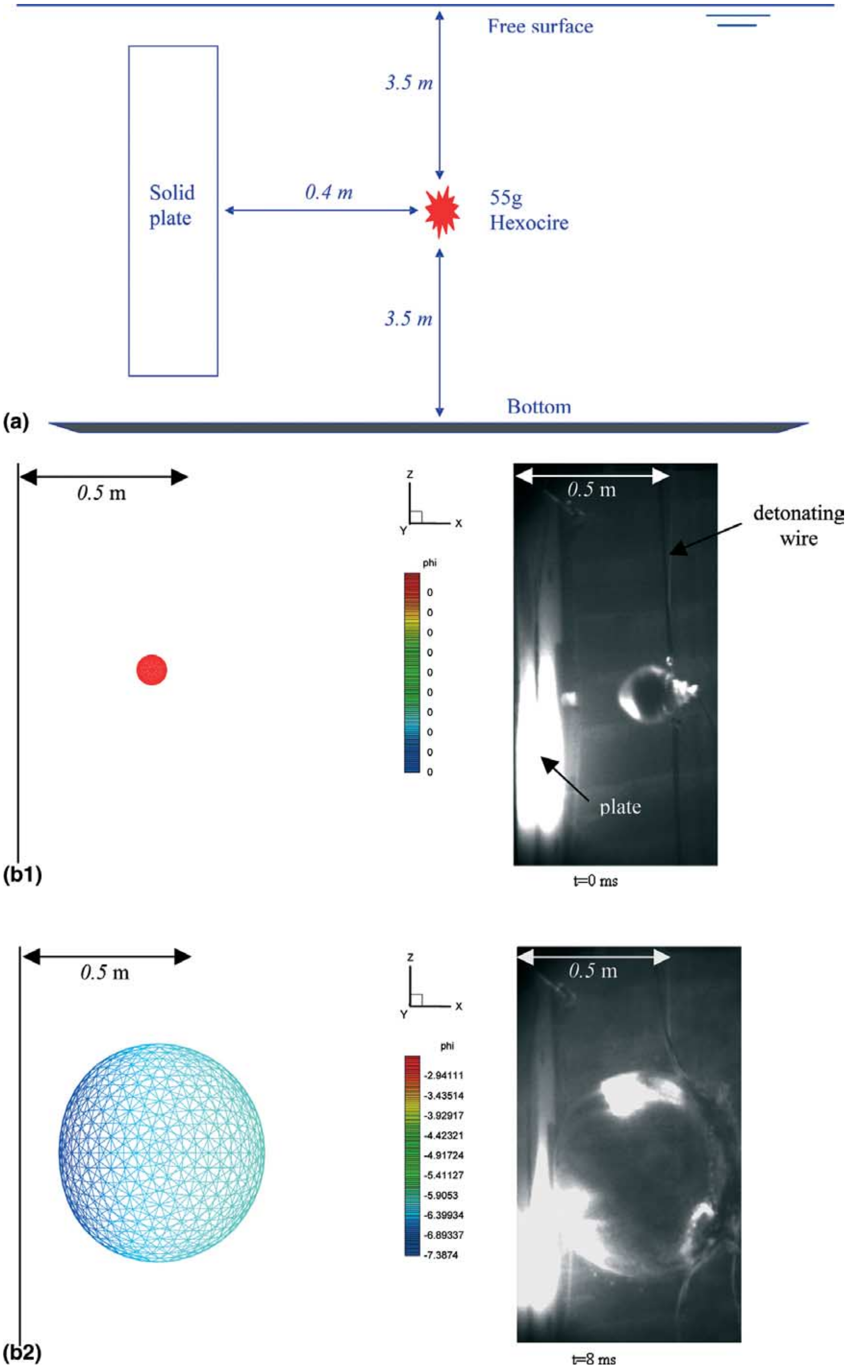

Fig. 12. (a) Configuration of explosion bubble near a vertical wall. b(1) Explosion bubble near a wall ($t = 0.00$ ms). b(2) Explosion bubble near a wall ($t = 7.82$ ms). b(3) Explosion bubble near a wall ($t = 50.00$ ms). b(4) Explosion bubble near a wall ($t = 77.69$ ms). b(6) Explosion bubble near a wall ($t = 90.57$ ms). b(7) Explosion bubble near a wall ($t = 93.34$ ms). b(8) Explosion bubble near a wall ($t = 97.50$ ms).

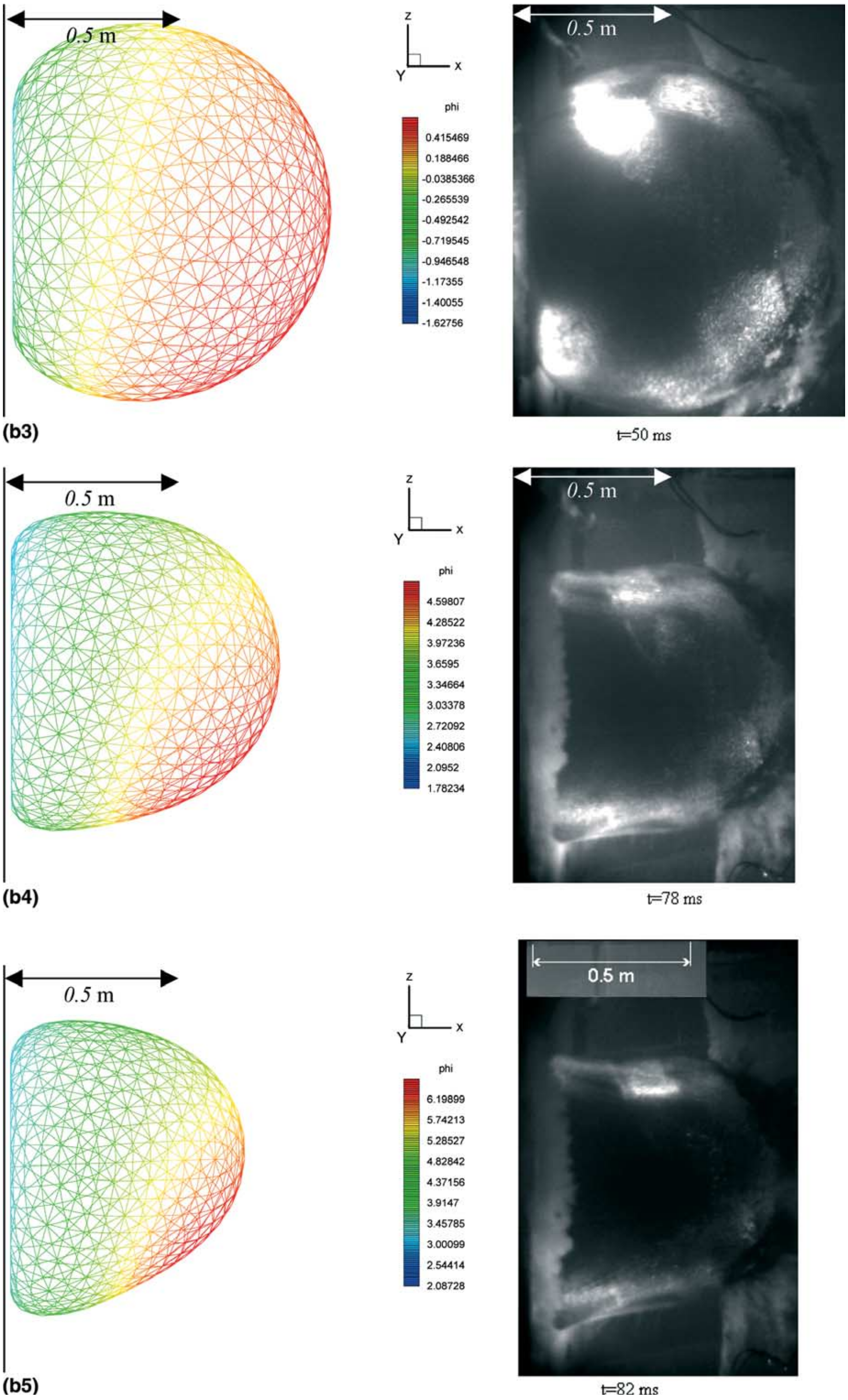

Fig. 12. (*continued*)

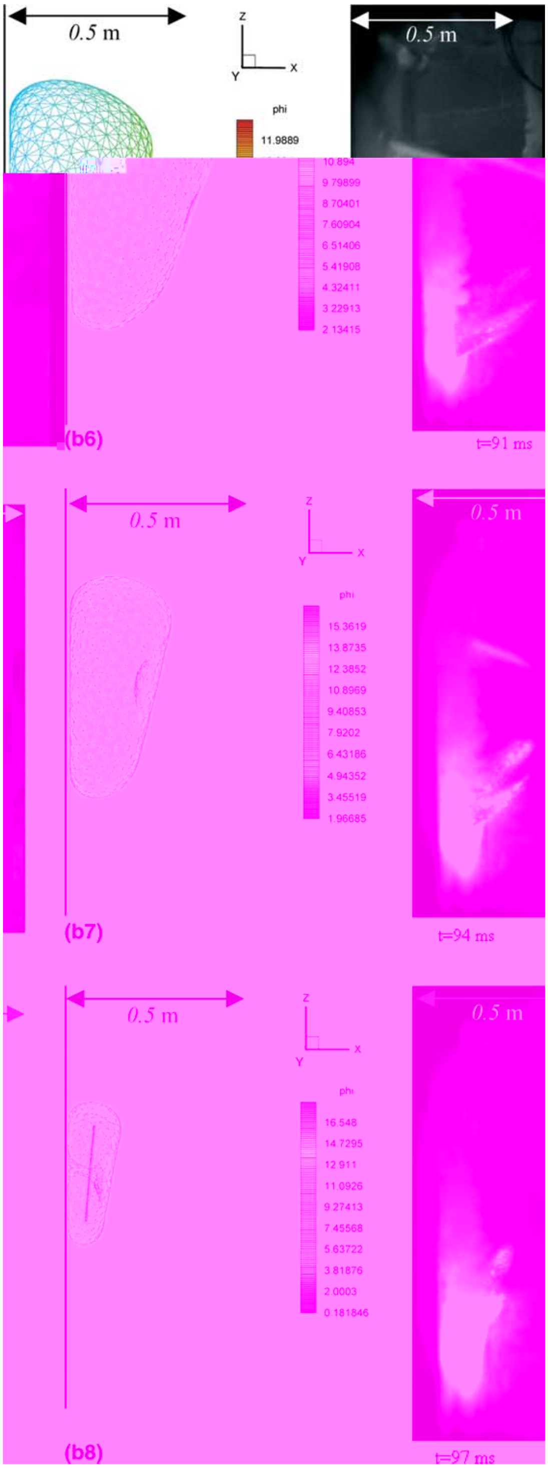

Fig. 12. (*continued*)

$$R_{\mathrm{m}} = 3.38\left(\frac{W}{H+10}\right)^{1/3}, \tag{22a}$$

$$\frac{R_0}{R_{\mathrm{m}}} = 0.0327H^{1/3}, \tag{22b}$$

$$P_0 = 13,9000\left(\frac{W}{V}\right)^{\lambda}, \tag{22c}$$

where $V = (4/3)\pi R_0^3$ is the initial bubble volume. Since the distances from the bubble to the free surface and bottom are large compared to the standoff distance to the vertical wall, the influences from both the free surface and bottom are ignored. The bubble is constructed by 1280 elements and the wall is made of 1152 elements. In the comparison, the bubble shape at the same (or nearest) time is used. Fig. 12b(1) shows the initial mesh and bubble size on the left with the color contour indicating the magnitude of the potential function. On the right side of the same figure, the image of the initial bubble from the experiment is shown. At around 8 ms, the bubble is still expanding. The influence of the left wall makes it slightly oval in shape (Fig. 12b(2)). At the time of 50 ms (Fig. 12b(3)), the bubble has about expanded to its maximum size. But because of the presence of the wall, its left side is clearly flattened. The bubble shape matches rather well with the image taken from the experiment. Fig. 12b(4) compares the bubble shape at the time of 78 ms. After reaching its maximum size, the bubble is in the process of collapsing. At around 82 ms the bubble collapses further which is depicted in Fig. 12b(5). Due to the effect of gravity, the bubble starts to lose its vertical symmetry at the time of 91 ms (Fig. 12b(6)). In the numerical model, a water jet can be observed to develop from the right side of the bubble surface. It is unfortunate that the experiment could not depict the happenings within the bubble; the diametrical view is blocked by the front surface of the bubble. In Fig. 12b(7) at 94 ms, the oblique water jet is just at about the quarter way mark towards making impact on the opposite side of the bubble surface. On the corresponding experimental image on the right, although one cannot see the development of the jet it is clear that the right side of the bubble surface has moved towards the steel plate on the left. At around 97 ms as shown in Fig. 12b(8), the bubble is already in a toroidal form (the purple bar inside the bubble is the vortex ring). The experimental image has depicted further movement of the bubble surface on the right side towards the left. Overall, the corresponding images from the experiment bear reasonable resemblance to the simulated results.

5. Conclusions

In this work, a 3D IBEM approach is presented to study underwater explosion bubble problems. The dynamics of bubble(s) in six different arrangements have been simulated. For the simplest Rayleigh bubble case strict comparison is made with the analytical solution of Rayleigh equation, and there is very good agreement. The energy balance for the evolution of the Rayleigh bubble is found to be effectively constant throughout the bubble evolution for at least two full cycles. In the buoyancy driven rising bubble case, the trajectories of the bubble centers in different gravity field are obtained and compared. For the remaining two cases of two initiating bubbles along a vertical line without gravity and along a horizontal line under a free surface with the effect of gravity included, it is found that the total energy of the respective simulation indicates an almost constant value throughout the evolution. Finally, the behavior of a bubble next to a rigid spherical ball in the vicinity of the free surface and separately near a rigid vertical wall are calculated. For the latter, the simulated results compared well to an underwater explosion experiment. All the above suggests that the present approach using IBEM is reasonably accurate. No smoothing algorithm has been applied and yet the results obtained are reasonably smooth for all the cases considered, which suggests that IBEM proposed is stable and robust.

Acknowledgements

We wish to acknowledge the contribution of Dr. P. Boyce and Dr. S. Debono from Centre Technique Des Systèmes Navals, France, who provided us the experimental photographs. We also want to acknowledge the discussions we had with Dr. K.S. Yeo of National University of Singapore in the course of preparing this manuscript.

Appendix A. Integration formulae over triangular elements

The triangular element ΔABC is displayed in Fig. 13. The source is distributed on the triangular element. The control point P is located at a distant of z above point A. The normal vector $\mathbf{n}$ of element ΔABC is pointing outward from the paper plane.

The induced potential at control point P by an uniform source distribution over triangular element ΔABC can be formulated as

$$\int_0^{\alpha+\beta}\int_0^{h\sec(\theta-\beta)} \frac{1}{\sqrt{r^2+z^2}} r\,\mathrm{d}r\,\mathrm{d}\theta = h\left[\operatorname{arctanh}\left(\frac{h\sin\alpha}{\sqrt{h^2+z^2\cos^2\alpha}}\right)+\operatorname{arctanh}\left(\frac{h\sin\beta}{\sqrt{h}^2+z^2\cos^2\beta}\right)\right]$$
$$+|z|\left[\arctan\left(\frac{|z|\sin\alpha}{\sqrt{h^2+z^2\cos^2\alpha}}\right)+\arctan\left(\frac{|z|\sin\beta}{\sqrt{h^2+z^2\cos^2\beta}}\right)-(\alpha+\beta)\right]. \tag{A.1}$$

The induced potential at control point P by a linear source distribution of which the highest source density 1 is located at point A, B and C of the triangular element ΔABC can be formulated as Eqs. (A.2), (A.3) and (A.4), respectively. These are

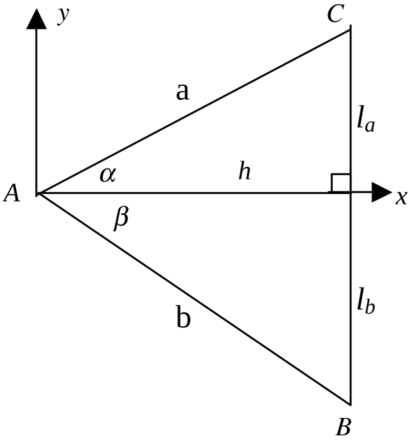

Fig. 13. Triangular element.

$$\begin{aligned}
&\int_0^{\alpha+\beta}\int_0^{h\sec(\theta-\beta)} \frac{1-(r/h)\cos(\theta-\beta)}{\sqrt{r^2+z^2}}\, r\,\mathrm{d}r\,\mathrm{d}\theta \\
&\quad= \frac{h^2-z^2}{2h}\left[\operatorname{arctanh}\left(\frac{h\sin\alpha}{\sqrt{h^2+z^2\cos^2\alpha}}\right)+\operatorname{arctanh}\left(\frac{h\sin\beta}{\sqrt{h^2+z^2\cos^2\beta}}\right)\right] \\
&\qquad+|z|\left[\arctan\left(\frac{|z|\sin\alpha z}{\sqrt{h^2+z^2\cos^2\alpha}}\right)+\arctan\left(\frac{|z|\sin\beta z}{\sqrt{h^2+z^2\cos^2\beta}}\right)-(\alpha+\beta)\right] \\
&\qquad+\frac{z^2}{2h}\left[\sin\alpha\ln\frac{h+\sqrt{h^2+z^2\cos^2\alpha}}{|z|\cos\alpha}+\sin\beta\ln\frac{h+\sqrt{h^2+z^2\cos^2\beta}}{|z|\cos\beta}\right],
\end{aligned} \tag{A.2}$$

$$\begin{aligned}
&\int_0^{\alpha+\beta}\int_0^{h\sec(\theta-\beta)} \frac{r\sin(\alpha+\beta-\theta)}{b\sin(\alpha+\beta)\sqrt{r^2+z^2}}\, r\,\mathrm{d}r\,\mathrm{d}\theta \\
&\quad= \frac{1}{h\sin(\alpha+\beta)}\left\{\frac{h^2+z^2}{2h}\sin\alpha\cos\beta\left[\operatorname{arctanh}\left(\frac{h\sin\alpha}{\sqrt{h^2+z^2\cos^2\alpha}}\right)\right.\right. \\
&\qquad\left.+\operatorname{arctanh}\left(\frac{h\sin\beta}{\sqrt{h^2+z^2\cos^2\beta}}\right)\right]+\frac{h}{2}\cos\alpha\cos\beta\left[\sqrt{h^2\sec^2\beta+z^2}-\sqrt{h^2\sec^2\alpha+z^2}\right] \\
&\qquad\left.+\frac{z^2}{2}\cos\beta\left[\cos(\alpha+\beta)\ln\frac{h+\sqrt{h^2+z^2\cos^2\beta}}{|z|\cos\beta}-\ln\frac{h+\sqrt{h^2+z^2\cos^2\alpha}}{|z|\cos\alpha}\right]\right\},
\end{aligned} \tag{A.3}$$

$$\begin{aligned}
&\int_0^{\alpha+\beta}\int_0^{h\sec(\theta-\beta)} \frac{r\sin\theta}{b\sin(\alpha+\beta)\sqrt{r^2+z^2}}\, r\,\mathrm{d}r\,\mathrm{d}\theta \\
&\quad= \frac{1}{h\sin(\alpha+\beta)}\left\{\frac{h^2+z^2}{2h}\sin\alpha\cos\beta\left[\operatorname{arctanh}\left(\frac{h\sin\alpha}{\sqrt{h^2+z^2\cos^2\alpha}}\right)\right.\right. \\
&\qquad\left.+\operatorname{arctanh}\left(\frac{h\sin\beta}{\sqrt{h^2+z^2\cos^2\beta}}\right)\right]+\frac{h}{2}\cos\alpha\cos\beta\left[\sqrt{h^2\sec^2\beta+z^2}-\sqrt{h^2\sec^2\alpha+z^2}\right] \\
&\qquad\left.+\frac{z^2}{2}\cos\beta\left[\cos(\alpha+\beta)\ln\frac{h+\sqrt{h^2+z^2\cos^2\beta}}{|z|\cos\beta}-\ln\frac{h+\sqrt{h^2+z^2\cos^2\alpha}}{|z|\cos\alpha}\right]\right\}.
\end{aligned} \tag{A.4}$$

On the other hand, the induced normal velocity at control point P by an uniform source distribution over triangular element ΔABC can be formulated as

$$\int_0^{\alpha+\beta}\int_0^{h\sec(\theta-\beta)} \frac{z\mathbf{n}}{\sqrt{r^2+z^2}}\, r\,\mathrm{d}r\,\mathrm{d}\theta = \frac{z\mathbf{n}}{|z|}\left[\alpha+\beta-\arctan\left(\frac{|z|\sin\alpha}{\sqrt{h^2+z^2\cos^2\alpha}}\right)-\arctan\left(\frac{|z|\sin\beta}{\sqrt{h^2+z^2\cos^2\beta}}\right)\right]. \tag{A.5}$$

The induced normal velocity at control point P by a linear source distribution of which the highest source density 1 is located at point A, B and C of the triangular element ΔABC can then be formulated as Eqs. (A.6), (A.7) and (A.8), respectively. These are

$$\int_0^{\alpha+\beta}\int_0^{h\sec(\theta-\beta)} \frac{1-(r/h)\cos(\theta-\beta)}{\left(\sqrt{r^2+z^2}\right)}\mathbf{n}zr\,\mathrm{d}r\,\mathrm{d}\theta$$
$$= \frac{z\mathbf{n}}{|z|}\left[\alpha+\beta-\operatorname{arctanh}\left(\frac{|z|\sin\alpha}{\sqrt{h^2+z^2\cos^2\alpha}}\right)-\operatorname{arctanh}\left(\frac{|z|\sin\beta}{\sqrt{h^2+z^2\cos^2\beta}}\right)\right]$$
$$+\frac{z\mathbf{n}}{h}\left[\operatorname{arctanh}\left(\frac{h\sin\alpha}{\sqrt{h^2+z^2\cos^2\alpha}}\right)+\operatorname{arctanh}\left(\frac{h\sin\beta}{\sqrt{h^2+z^2\cos^2\beta}}\right)\right.$$
$$\left.-\sin\alpha\ln\frac{h+\sqrt{h^2+z^2\cos^2\alpha}}{|z|\cos\alpha}-\sin\beta\ln\frac{h+\sqrt{h^2+z^2\cos^2\beta}}{|z|\cos\beta}\right], \tag{A.6}$$

$$\int_0^{\alpha+\beta}\int_0^{h\sec(\theta-\beta)} \frac{r\sin\alpha+\beta-\theta}{b\sin(\alpha+\beta)\sqrt{r^2+z^2}}z\mathbf{n}r\,\mathrm{d}r\,\mathrm{d}\theta$$
$$=\frac{-z\mathbf{n}}{h\sin(\alpha+\beta)}\times\left\{\sin\alpha\cos\beta\left[\operatorname{arctanh}\left(\frac{h\sin\alpha}{\sqrt{h^2+z^2\cos^2\alpha}}\right)+\operatorname{arctanh}\left(\frac{h\sin\beta}{\sqrt{h^2+z^2\cos^2\beta}}\right)\right]\right.$$
$$\left.+\cos\beta\left[\cos(\alpha+\beta)\ln\frac{h+\sqrt{h^2+z^2\cos^2\beta}}{|z|\cos\beta}-\ln\frac{h+\sqrt{h^2+z^2\cos^2\alpha}}{|z|\cos\alpha}\right]\right\}, \tag{A.7}$$

$$\int_0^{\alpha+\beta}\int_0^{h\sec(\theta-\beta)} \frac{r\sin\theta}{b\sin(\alpha+\beta)\sqrt{r^2+z^2}}z\mathbf{n}r\,\mathrm{d}r\,\mathrm{d}\theta$$
$$=\frac{-z\mathbf{n}}{h\sin(\alpha+\beta)}\times\left\{\sin\alpha\cos\beta\left[\operatorname{arctanh}\left(\frac{h\sin\alpha}{\sqrt{h^2+z^2\cos^2\alpha}}\right)+\operatorname{arctanh}\left(\frac{h\sin\beta}{\sqrt{h^2+z^2\cos^2\beta}}\right)\right]\right.$$
$$\left.+\cos\beta\left[\cos(\alpha+\beta)\ln\frac{h+\sqrt{h^2+z^2\cos^2\beta}}{|z|\cos\beta}-\ln\frac{h+\sqrt{h^2+z^2\cos^2\alpha}}{|z|\cos\alpha}\right]\right\}. \tag{A.8}$$

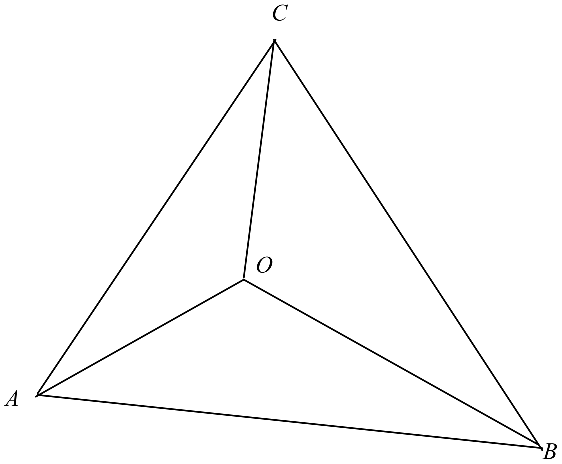

Fig. 14. Sub-division of triangular elements.

The induced potential at control point A by a linear source distribution on the border BC of which the highest source density 1 is located at point $B(A)$ can be formulated as Eqs. (A.9), (A.10). These are

$$\int_{-l_b}^{l_a} \frac{1}{\sqrt{x^2+h^2}} \frac{l_a - x}{l_a + l_b} \mathrm{d}x = \frac{1}{\sin(\alpha+\beta)} \left[\sin\alpha\cos\beta \ln\frac{(1+\sin\alpha)(1+\sin\beta)}{\cos\alpha\cos\beta} + \cos\alpha - \cos\beta \right], \tag{A.9}$$

$$\int_{-l_b}^{l_a} \frac{1}{\sqrt{x^2+h^2}} \frac{x + l_b}{l_a + l_b} \mathrm{d}x = \frac{1}{\sin(\alpha+\beta)} \left[\sin\beta\cos\alpha \ln\frac{(1+\sin\alpha)(1+\sin\beta)}{\cos\alpha\cos\beta} + \cos\beta - \cos\alpha \right]. \tag{A.10}$$

If the perpendicular projection O of the control point on the triangular element ΔABC does not coincide with the corners A, B or C, then the triangular element is divided into three smaller triangular elements ΔOAB, ΔOBC and ΔOCA (see Fig. 14). For each sub-triangular element, the above formulae can be applied.

References

[1] J.P. Best, The formation of toroidal bubbles upon the collapse of the transient cavities, J. Fluid Mech. 251 (1993) 79–107.

[2] J.R. Blake, J.M. Boulton-Stone, R.P. Tong, Boundary integral methods for rising, bursting and collapsing bubbles, in: H. Power (Ed.), BE Applications in Fluid Mechanics, vol. 4, Computational Mechanics Publications, Southampton, 1995, pp. 31–72.

[3] J.R. Blake, D.C. Gibson, Growth and collapse of a vapour cavity near a free surface, J. Fluid Mech. 111 (1981) 123–140.

[4] J.R. Blake, D.C. Gibson, Cavitation bubbles near boundaries, Annu. Rev. Fluid Mech. 19 (1) (1987) 99–123.

[5] J.R. Blake, B.B. Taib, G. Doherty, Transient cavities near boundaries. Part 1. Rigid boundary, J. Fluid Mech. 170 (1986) 479–497.

[6] J.M. Boulton-Stone, A comparison of boundary integral methods for studying the motion of a two-dimensional bubble in an infinite fluid, Comput. Methods Appl. Mech. Eng. 102 (1993) 213–234.

[7] P. Boyce, S. Debono, Report of underwater explosion tests, Centre Technique Des Systeme Navals, France, 2003.

[8] G.L. Chahine, T.O. Perdue, C.B. Tucker, Interaction between an underwater explosion bubbles and a solid submerged body, Tech. Rep. 86029-1, Traycor Hydronautics Inc., 1988.

[9] P.J. Harris, A numerical model for determining the motion of bubble close to a fixed rigid structure in a fluid, Int. J. Numer. Methods Eng. 33 (9) (1992) 1813–1822.

[10] T.S. Lundgren, M.N. Mansour, Vortex ring bubbles, J. Fluid Mech. 224 (1991) 177–196.

[11] H.N. Oguz, A. Prosperetti, Bubble entrainment by the impact of drops on liquid surfaces, J. Fluid Mech. 219 (1990) 143–179.

[12] R.P. Tong, A new approach to modeling an unsteady free surface in boundary integral methods with application to bubble-structure interactions, Math. Comput. Simulation 44 (4) (1997) 415–426.

[13] C. Wang, B.C. Khoo, K.S. Yeo, Elastic mesh technique for 3D BIM simulation with an application to underwater explosion bubble dynamics, Comput. Fluids 32 (9) (2003) 1195–1212.

[14] Q.X. Wang, K.S. Yeo, B.C. Khoo, K.Y. Lam, Nonlinear interaction between gas bubble and free surface, Comput. Fluids 25 (7) (1996) 607–628.

[15] S.A. Wilkerson, A boundary integral approach to three dimensional underwater explosion bubble dynamics, Dissertation, Department of Mechanical Engineering, The Johns Hopkins University, 1990.

[16] S.G. Zhang, J.H. Duncan, On the non-spherical collapse and rebound of, Phys. Fluids 6 (7) (1994) 2352–2362.

[17] S.G. Zhang, J.H. Duncan, G.L. Chahine, The final stage of the collapse of a cavitation bubble near a rigid wall, J. Fluid Mech. 257 (1993) 147–181.

[18] Y.L. Zhang, K.S. Yeo, B.C. Khoo, W.K. Chong, Three-dimensional computation of bubbles near a free surface, J. Comput. Phys. 146 (1) (1998) 105–123.

[19] Y.L. Zhang, K.S. Yeo, B.C. Khoo, W.K. Chong, Simulation of three-dimensional bubbles using desingularized boundary integral method Int., J. Numer. Methods Fluids 31 (8) (1999) 1311–1320.

[20] Y.L. Zhang, K.S. Yeo, B.C. Khoo, C. Wang, 3D jet impact and toroidal bubbles, J. Comput. Phys. 166 (2) (2001) 336–360.